Transient Eddy Kinetic Energetics on Mars in Three Reanalysis Datasets

J. MICHAEL BATTALIO[a]

[a] *Department of Earth and Planetary Sciences, Yale University, New Haven, Connecticut*

(Manuscript received 8 February 2021, in final form 20 September 2021)

ABSTRACT: The ability of Martian reanalysis datasets to represent the growth and decay of short-period ($1.5 < P < 8$ sol) transient eddies is compared across the Mars Analysis Correction Data Assimilation (MACDA), Open access to Mars Assimilated Remote Soundings (OpenMARS), and Ensemble Mars Atmosphere Reanalysis System (EMARS). Short-period eddies are predominantly surface based, have the largest amplitudes in the Northern Hemisphere, and are found, in order of decreasing eddy kinetic energy amplitude, in Utopia, Acidalia, and Arcadia Planitae in the Northern Hemisphere, and south of the Tharsis Plateau and between Argyre and Hellas basins in the Southern Hemisphere. Short-period eddies grow on the upstream (western) sides of basins via baroclinic energy conversion and by extracting energy from the mean flow and long-period ($P > 8$ sol) eddies when interacting with high relief. Overall, the combined impact of barotropic energy conversion is a net loss of eddy kinetic energy, which rectifies previous conflicting results. When Thermal Emission Spectrometer observations are assimilated (Mars years 24–27), all three reanalyses agree on eddy amplitude and timing, but during the Mars Climate Sounder (MCS) observational era (Mars years 28–33), eddies are less constrained. The EMARS ensemble member has considerably higher eddy generation than the ensemble mean, and bulk eddy amplitudes in the deterministic OpenMARS reanalysis agree with the EMARS ensemble rather than the EMARS member. Thus, analysis of individual eddies during the MCS era should only be performed when eddy amplitudes are large and when there is agreement across reanalyses.

SIGNIFICANCE STATEMENT: Dust storms on Mars are initiated by traveling atmospheric waves, so understanding the relationships between waves and dust is critical to surface spacecraft safety. The growth and decay of waves are compared in three datasets to evaluate whether waves behave consistently across datasets and are represented similarly across different eras of instrumentation. Waves grow by instabilities caused by horizontal and vertical temperature gradients and lose energy to slower-traveling waves at higher altitudes, but agreement across datasets declines using more recent observations because of problems measuring temperatures near the surface. Regardless, combining dust storm observations and descriptions of traveling waves provides a new avenue for explaining dust storm variability on Mars.

KEYWORDS: Eddies; Extratropical cyclones; Planetary atmospheres; Reanalysis data

1. Introduction

The yearly cycle of dust on Mars exhibits considerable seasonal uniformity, excluding global dust events (GDEs), with a relatively low-opacity season occurring during northern spring and summer and a dusty season during northern fall and winter (Montabone et al. 2015; Kass et al. 2016; Montabone et al. 2020; Battalio and Wang 2021); however, within those seasons, interannual variability reigns on shorter time scales, in the 1–30 sol (Mars days) range (Battalio and Wang 2021). The difference in seasonal and weekly to monthly dust variability rests on the nature of transient waves that help initiate dust storms (Wang et al. 2003; Cantor 2007; Hollingsworth and Kahre 2010; Hinson and Wang 2010; Hinson et al. 2012; Wang and Richardson 2015; Xiao et al. 2019; Battalio and Wang 2019, 2020, 2021). Transient waves occur most strongly in northern fall and winter (Barnes 1980; Wilson et al. 2002; Banfield et al. 2004; Mooring and Wilson 2015; Lewis et al. 2016) but have considerable interannual variability in wavenumber and amplitude (Collins et al. 1996; Greybush et al. 2019a). Thus, better understanding the nature of transient waves relates to explaining the variability of dust storms.

Corresponding author: J. Michael Battalio, michael@battalio.com

a. Martian transient wave climatology

Transient waves in the Martian atmosphere exhibit periods of approximately 7, 3, and 2 sols in the Northern Hemisphere (Barnes 1980, 1981), associated with wavenumbers 1, 2, and 3, respectively (Banfield et al. 2004). Transient eddies below 20 km are tilted westward with height, feed off poleward and vertical heat fluxes, and are driven by baroclinic processes (Barnes 1984; Barnes et al. 1993; Read and Lewis 2004; Barnes et al. 2017). Northern eddies amplify along 40°–70°N, within the low-lying Planitae around 90°, 180°, and 330°E (Hollingsworth and Barnes 1996; Hollingsworth et al. 1997). Different wavenumbers maximize at different altitudes. In eddy temperatures, wavenumber 1 is deepest, followed by wavenumber 2, and wavenumber 3 is confined to the lowest scale height (<10 km) (Greybush et al. 2019a). Wave amplitude generally increases with wavenumber from 1 to 2 to 3 (Greybush et al. 2019a; Battalio and Wang 2020; Hinson and Wilson 2021). In the Southern Hemisphere, wave amplitudes are less than one-quarter that of the Northern Hemisphere (20 vs 4 K) with a discernible wavenumber-4 component (Barnes et al. 1993; Banfield et al. 2004; Greybush et al. 2012; Mooring and Wilson 2015).

Transient eddies follow a distinct yearly climatology. Near-surface eddies amplify in fall and late winter along the temperature gradient maximum near the edge of the polar ice cap

DOI: 10.1175/JAS-D-21-0038.1

that migrates from 40° to 90°N/S, aligning with the times of recurring major dust storms at the same season (Wang et al. 2013; Kass et al. 2016; Battalio and Wang 2019, 2020, 2021). A lull in eddy amplitude occurs at winter solstice, called the solstitial pause (Lewis et al. 2016), similar to the Pacific midwinter minimum (Nakamura 1992). The Northern Hemisphere pause occurs at $L_s \approx 240°–300°$, and the southern pause occurs around $L_s \approx 60°–120°$.[1] The solstitial pauses occur every year, but there is interannual variability, especially in the Northern Hemisphere, depending on exactly when the northern autumnal regional dust storm begins (Kass et al. 2016). Northern transient eddies instigate dust activity that flushes into the Southern Hemisphere (Wang et al. 2013; Battalio and Wang 2021). Once dust opacity increases, warming of the middle atmosphere stabilizes against the baroclinic instability that drives transient eddies (Kuroda et al. 2007; Battalio et al. 2016; Battalio and Wang 2020). Radiatively active clouds may also contribute to the solstitial pause by altering the vertical temperature profile and baroclinicity (Mulholland et al. 2016; Lee et al. 2018).

b. Eddy energetics

Eddy energetics, including the generation, transport, and conversion of eddy kinetic energy, provides a vital tool to understanding storm track dynamics on Earth (e.g., Chang et al. 2002). Generally, baroclinic eddies follow the same downstream development, baroclinic growth (conversion of eddy kinetic energy from zonal-mean available potential energy), and barotropic decay (loss of kinetic energy to the mean flow or other eddy frequencies), modulated by the individual circumstances of their particular storm track, such as topography and the strength of temperature gradients.

Martian eddies behave in a similar way to those on Earth, as diagnosed in the Orlanski and Katzfey (1991) paradigm, in that they are initiated via ageostrophic geopotential flux (AGF) convergence and grow through baroclinic instability (Battalio et al. 2016, 2018b). However, the role of barotropic energy conversion in the downstream propagating wave depends on the local topography: it is a source of eddy kinetic energy (EKE) in a channel north of the Tharsis Plateau (~95°W), but in the basins (Planitae), barotropic conversion is a sink of EKE. Overall, exchange between the mean flow and eddies appears to be a source of EKE (Battalio et al. 2016, 2018a,b), and waves have a mixed baroclinic–barotropic character (Barnes et al. 1993; Hinson 2006).

Barotropic instabilities acting as a source of transient wave energy is somewhat puzzling, as it is contrary to Earth's case and that found using other energetics analyses for Mars. Investigating energetics using the forms of Ulbrich and Speth (1991) and Hayashi and Golder (1983), barotropic conversion is a sink of EKE (Wang et al. 2013; Wang and Toigo 2016). Eddy energetics analysis can be further placed into context of the global atmospheric energy cycle using the global energy cycle. For Mars, baroclinic instability is a global eddy energy source, and barotropic conversion is positive so that friction is the only EKE sink (Tabataba-Vakili et al. 2015).

Given the conflicting results about the nature of transient eddies on Mars, the goals of the present work are threefold: First, present the multiyear energetics of Martian transient waves; second, compare the representation of transient eddies across three reanalyses and two instrumental eras; and third, unify the disparate results of eddy energetics analysis for Mars.

2. Methods and data

a. Mars reanalysis datasets

The oldest available Martian atmospheric reanalysis is the Mars Analysis Correction Data Assimilation (MACDA v1.0; Montabone et al. 2014). MACDA is generated from observations from the Thermal Emission Spectrometer (TES; Smith 2004) on board the Mars Global Surveyor during the period from $L_s = 141°$, Mars year (MY) 24 to $L_s = 86°$, MY 27. TES captures twice-daily (approximately 0200 and 1400 local Mars time) nadir temperature profiles from the surface to ~40 km on 21 vertical levels. Daily column dust opacities are also captured, but when no dust observations are available, persistence is assumed until new observations are available. These observations are assimilated using an analysis correction scheme (Lewis et al. 2007) into the U.K. version of the LMD Mars Global Circulation Model (MGCM) (Forget et al. 1999). MACDA has a $5° \times 5°$ regular horizontal grid with 25 sigma levels every two Mars hours. The TES observations that are assimilated have shown some biases due to poor temperature retrievals in MY 26 (Pankine 2015, 2016), but TES observations yield improved dynamics versus free model runs (Waugh et al. 2016).

The Open access to Mars Assimilated Remote Soundings (OpenMARS v1.0; Holmes et al. 2020) assimilates TES retrievals from $L_s = 98°$, MY 24 to $L_s = 86°$, MY 27 and follows the same procedure as MACDA for assimilating data during the TES era, using the same assimilation method (Lewis et al. 2007) and an updated version of the same MGCM (Forget et al. 1999). OpenMARS also extends from $L_s = 108°$, MY 28 to $L_s = 278°$, MY 29 and from $L_s = 19°$, MY 30 to $L_s = 351°$, MY 32 using observations from the Mars Climate Sounder (MCS; Kleinböhl et al. 2009), on board the Mars Reconnaissance Orbiter. MCS captures twice-daily (approximately 0300 and 1500 local Mars time) along-track limb profiles of temperature with 105 vertical levels, but the sensitivity is reduced in the lowest 5–10 km of the atmosphere (Greybush et al. 2019a). Column dust opacity from TES and MCS is also assimilated in a similar way as MACDA. OpenMARS is on a $5° \times 5°$ horizontal grid with 25 sigma levels every two Mars hours.

The Ensemble Mars Atmosphere Reanalysis System (EMARS v1.0; Greybush et al. 2019b) is an ensemble dataset with 16 members. EMARS uses a local ensemble transform Kalman filter to assimilate data (Greybush et al. 2012, 2019a) into the Geophysical Fluid Dynamics Laboratory MGCM (Wilson and Hamilton 1996) at 6° longitude × 5° latitude horizontal resolution with 28 hybrid sigma-pressure levels at hourly temporal resolution. EMARS extends slightly longer

[1] The L_s, or areocentric longitude, is a measure of time of year; $L_s = 0°$ is northern spring, $L_s = 90°$ is northern summer, etc.

during the TES era than MACDA or OpenMARS to include more sporadic observations before the instrument ceased operation. EMARS assimilates dust from the Mars Climate Database, version 5, dust scenario (Montabone et al. 2015), which includes available TES, MCS, and Thermal Emission Imaging System (THEMIS) dust retrievals from Mars Odyssey (Smith 2009). The ensemble mean and a single ensemble member from the EMARS dataset are available, and both are analyzed for comparison. The ensemble is generated by varying the dust opacity uniformly from 0.7 to 1.3 times the amount specified by the observation dataset and by alternating the water ice cloud radiative properties across three values (Greybush et al. 2019b). The single member has the median amount of dust opacity and water ice cloud forcing and hereinafter will be referred to as the EMARS member. The EMARS-TES era spans from $L_s = 103°$, MY 24 to $L_s = 102°$, MY 27, and the EMARS-MCS era spans from $L_s = 112°$, MY 28 to $L_s = 105°$, MY 33 using along-track limb retrievals of temperature, dust, and water ice from MCS.

b. *Calculation of eddies*

Eddies are filtered in two steps. First, the total eddy components are defined by removing the 60-sol running mean (30 sols on either side of a given time step); this distinguishes time-mean and eddy components with a cutoff of $P = 60$ sols. The running-mean window is selected to be larger than the time scale of synoptic-scale transient eddies but not long enough to include very long-period, nonstationary eddies (Battalio and Wang 2020).

Second, the $P < 60$-sol eddy component is further filtered to $1.5 < P < 8$ sol using a hamming-window filter (Battalio et al. 2016, 2018b; Battalio and Wang 2020) to remove the semidiurnal and diurnal tides and to allow for the quantification of energy transfer between eddies of different periods. The lower bound of 1.5 sols is selected to completely remove any tidal impacts but still include the shortest period transient eddies that have a period of $P \sim 2$ sols (Banfield et al. 2004). The upper bound reflects the longest period baroclinic eddies prevalent in the Northern Hemisphere (Battalio and Wang 2020). Raising the upper period bound for the filter does not substantively impact the results.

c. *Eddy kinetic energy equation*

The EKE equation (Orlanski and Katzfey 1991) is applied to assess local energetics of transient waves. The EKE equation relates the change in EKE to transport by advection, convergence of geopotential height, and to the baroclinic and barotropic conversion of energy:

$$\frac{\partial}{\partial t}\langle K_e\rangle = \overbrace{-\langle\nabla_3\cdot\mathbf{v}_3K_e\rangle}^{1}\overbrace{-\langle\nabla_3\cdot\mathbf{v}'_3\phi'\rangle}^{2}\overbrace{-\langle\omega'\alpha'\rangle}^{3}\overbrace{-\langle\mathbf{v}'\cdot(\mathbf{v}'_3\cdot\nabla_3)\overline{\mathbf{v}}\rangle}^{4}\overbrace{+\langle\mathbf{v}'\cdot\left[\left(\mathbf{v}_3^{\dagger}\cdot\nabla_3\right)\mathbf{v}^{\dagger}\right]\rangle}^{5}\overbrace{+\langle\frac{\tan(\psi)}{r}(u'u'\overline{v}-u'v'\overline{u}-u'\overline{u'v'}+v'\overline{u'u'})\rangle}^{6}$$
$$\overbrace{-\mathbf{v}'\cdot\tau'}^{7}\overbrace{+\epsilon}^{8}. \qquad (1)$$

The full wind vector and the horizontal components of the wind vector are $\mathbf{v}_3 = (u, v, \omega)$ and $\mathbf{v} = (u, v)$, respectively. The wave (eddy) components of the state variables ($P < 60$ sols) are denoted with daggers. The primed variables are the eddy components bandpass filtered by period ($1.5 < P < 8$ sol), and square brackets indicate bandpass filtering of an entire term. The EKE per unit mass is $K_e = (1/2)(u'^2 + v'^2)2$, ψ is latitude, ϕ is the geopotential height, $\alpha = 1/\rho$ is the specific volume, and τ is the aerodynamic stress. Terms with an overbar are averaged every 60 sols. Angle brackets denote a mass-weighted average over the pressure coordinate (Battalio et al. 2016; Battalio and Wang 2020).

Each term on the right-hand side describes a process that alters the time rate of change of the EKE. Term 1 is the advection of EKE by the whole flow (ETRANS). Term 2 is the ageostrophic geopotential flux (AGF) convergence, which represents the dispersion of EKE by the pressure work. Terms 1 + 2 will be collectively referred to as EKE flux convergence, which can be a local source or sink of EKE, but is a conserved term that ideally integrates to approximately zero over the volume of the atmosphere, assuming mass conservation. This term deviates from zero for several reasons. The EKE flux convergence is calculated in flux form to reduce numerical errors (Battalio et al. 2016; Battalio 2017) but is susceptible to errors caused by the conversion from sigma to pressure coordinates, errors in the calculated vertical velocities (section 2d), or numerical errors due to the coarseness of the reanalyses. The AGF convergence also captures the impact of mass transport through the lower boundary as a result of eddies inducing deposition or sublimation of the CO_2 ice cap, which is a uniquely Martian feature.

Term 3 is the baroclinic energy conversion (BCEC) and describes the conversion of eddy available potential energy to EKE. Terms 4 and 5 are both barotropic energy conversion (BTEC) terms whereby kinetic energy is transferred between the mean flow and the eddies and among different eddy periods. Term 4 is the shear generation term (Reynolds stress term) that describes the interaction between the gradient of the mean flow and the eddy momentum fluxes. Term 5 is the cross-frequency eddy interaction (CFEI) term and is the correlation of the eddy wind with the divergence of eddy flux. It represents the interaction between the bandpass filtered eddies of interest ($1.5 < P < 8$ sol) with the tides ($P < 1.5$ sol) and long-period eddies ($8 < P < 60$ sol). Term 6 is the curvature term and describes the impact of spherical geometry on the EKE. Its effects are the result of the coordinate system varying with the planetary surface. Term 7 describes the surface aerodynamic stress or surface drag (McLay and Martin

2002), representing the loss of EKE by friction with the surface; it is only calculated for the EMARS dataset. Term 8 is the residual ϵ and accounts for effects not explicitly calculated, for example, errors caused by the analysis increment (Chang 2000), dissipation, gravity wave stress, or in the case of the EMARS ensemble mean, Reynolds stresses associated with the spread of the ensemble about its mean. It is found by subtracting terms 1–6 for MACDA and OpenMARS and 1–7 for EMARS from the directly calculated EKE tendency. [For derivation of the EKE equation, see McLay and Martin (2002), Szunyogh (2014), or Park and Kim (2021).]

There is a relationship between the Reynolds stress term, CFEI, and curvature terms in local energetics when compared with the global energy cycle. Barotropic conversion in the global energy cycle formalism consists of the integral of multiple terms, including Reynolds stress and curvature (Oort 1964; Ulbrich and Speth 1991). In local energetics, the curvature term is treated as a separate entity as its existence is a byproduct of spherical geometry (McLay and Martin 2002). On Earth, the CFEI term can have a magnitude comparable to the Reynolds stress if the eddies are further decomposed into high-, intermediate-, and low-frequency eddies (Deng and Jiang 2011; Jiang et al. 2013). Thus, BTEC will be considered the sum of the Reynolds stresses, CFEI, and curvature [Eq. (1): terms 4, 5, and 6].

d. Calculation of vertical velocities and heights

The EMARS dataset contains the vertical velocity ω and the height above the surface h, but the MACDA and OpenMARS datasets do not. The geopotential height is obtained from the temperature. Vertical velocities are obtained using the extended version of the quasigeostrophic (QG) ω equation (Battalio and Dyer 2017). While only an approximation to the true vertical velocity, Mars lies in a dynamical regime that obeys quasigeostrophy except near the equator (Battalio et al. 2016, 2018b). The skill of QG-ω approximating the true atmospheric state is estimated by calculating QG-ω for the EMARS dataset. In the layer between 400 and 100 Pa and poleward of 20°, QG-ω and EMARS ensemble mean ω are correlated at ~0.8. The high correspondence decreases closer to the surface due to the no-normal flow boundary condition (Battalio and Dyer 2017). Correlations are also smaller near the equator due to Coriolis vanishing; however, most transient wave activity on Mars occurs away from the equator, so the energetics results are not overly impacted. Generally, QG-ω does a good job capturing the larger time-mean patterns of the vertical motion field, particularly around topography, like Tharsis, Arabia Terra, and the southern basins of Argyre and Hellas (not shown). Further, QG-ω matches the instantaneous vertical motion field for large-scale atmospheric features, like the transient eddies studied here. Most importantly, the correlation between the AGF and ETRANS terms calculated using the EMARS ensemble mean produced vertical velocity and QG-ω is ~0.95 and is ~0.75 for the BCEC and BTEC, depending on time of year. Thus, it is the quasigeostrophic part of ω is most important for calculating the eddy energetics (Battalio et al. 2016).

3. Results

The energetics results are discussed for the MCS and TES observation eras separately, as the observations have differing skill at constraining the underlying MGCMs of each reanalysis to a particular eddy solution (Greybush et al. 2019a,b). Further, results for the Northern and Southern Hemispheres are presented separately as transient eddies are more amplified in the Northern Hemisphere (Banfield et al. 2004). The focus is first placed on the similarities in the eddy energetics across datasets, investigating the temporal evolution, and then vertical and zonal spatial structures. Within this framework, the eddy energetics for a specific dust storm event is compared. The differences between observational eras and datasets are detailed in section 4.

a. Temporal evolution of eddy kinetic energy equation terms

The volume integrated (30°–90°N) $1.5 < P < 8$ sol (short-period) EKE and energy conversion terms are shown in Fig. 1. Eddy activity peaks before and after solstice during L_s = 180°–240° and L_s = 310°–10° within the TES era. Activity during the solstitial pause (L_s = 240°–310°) has an amplitude about one-third that of fall and late winter but is approximately double the EKE in the northern summer (L_s = 10°–180°). The largest individual peaks in EKE just precede or align with times of large dust events (Battalio and Wang 2020, 2021).

The BCEC evolution echoes the EKE, pointing to the baroclinic nature of these eddies. Individual peaks of BCEC align with those of EKE, for example, in MY 24 at L_s = 335°, MY 25 at L_s = 330°, or MY 26 at L_s = 210°. BCEC during the pause drops to near zero, with brief, small fluctuations to negative values. BCEC during northern summer remains fairly constant around zero in both the TES and MCS eras. BTEC is negative before (L_s = 180°–240°) and after (L_s = 300°–20°) the solstitial pause but becomes slightly positive during the pause itself.

While transient eddies in the Southern Hemisphere are weaker in amplitude than the Northern Hemisphere (Banfield et al. 2004; Lewis et al. 2016; Battalio et al. 2018b), eddy energetics does follow a similar seasonality around the southern winter solstice, albeit with reduced amplitudes of EKE and energy conversion (Fig. 2). However, BCEC and BTEC are larger in magnitude before and after the pause. The general pattern of strong eddy activity on either side of the winter solstice holds across all years, but while the Northern Hemisphere solstitial pause is essentially nonexistent during the MCS era, the Southern Hemisphere exhibits a small reduction in eddy activity during solstice.

The two transport terms, the AGF and ETRANS, are approximately zero in the hemispheric means for both the Northern and Southern Hemisphere (not shown). Because the ETRANS and the horizontal portion of the AGF can neither create nor destroy EKE, this indicates that each hemisphere is generally a closed system. There is no overall transfer of EKE from one hemisphere to the other; short-period EKE remains in the hemisphere in which it is

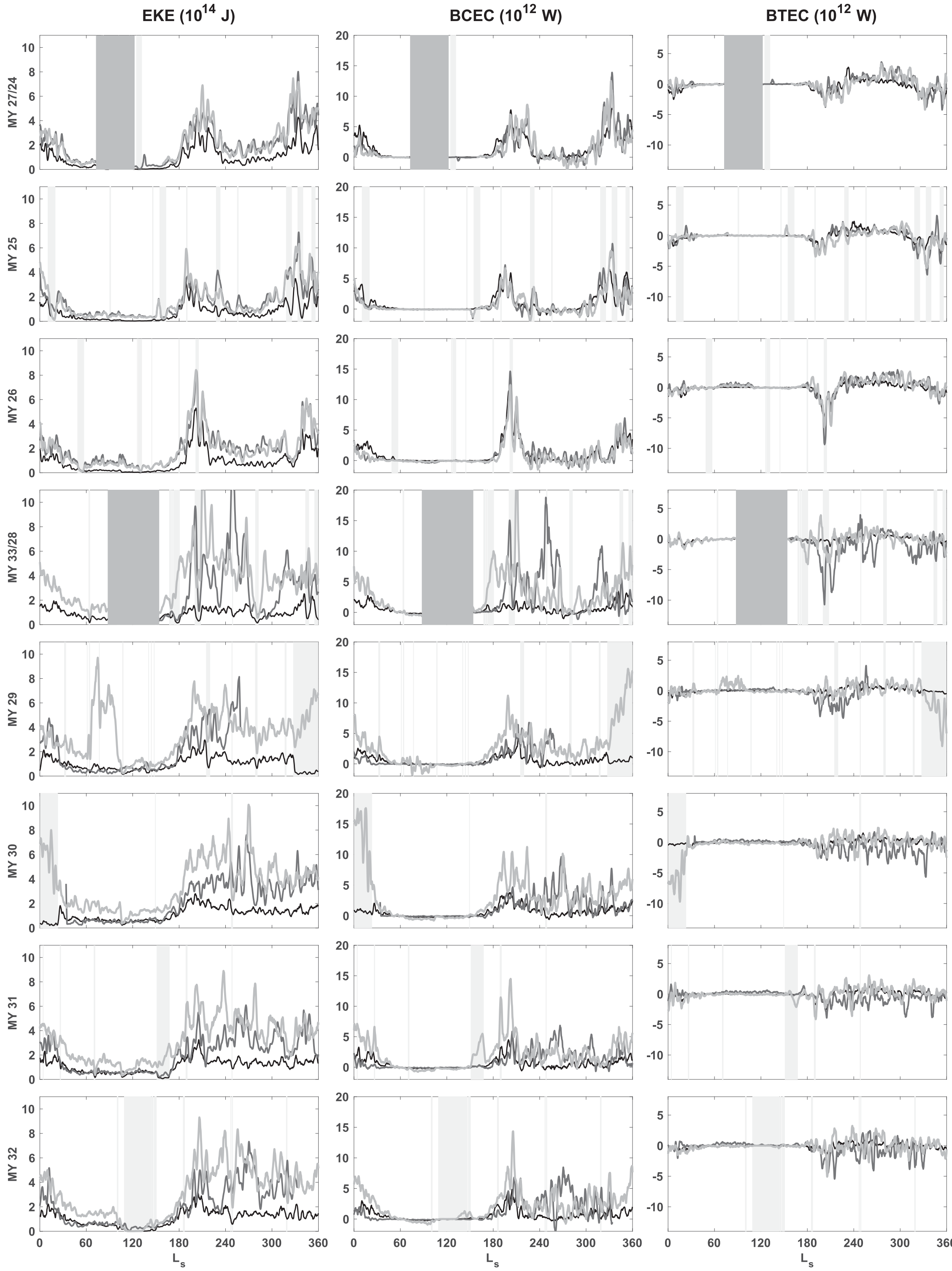

FIG. 1. Temporal evolution of the vertically and horizontally integrated (left) EKE, (center) BCEC, and (right) BTEC for $1.5 < P < 8$ sol eddies in the latitude band 30°–90°N. The black curve indicates EMARS, and dark gray indicates OpenMARS. The light-gray curve indicates MACDA in MY 24–27 and the single EMARS ensemble member in MY 28–33. Light-gray bars indicate when observations are unavailable, and dark-gray bars separate individual MY. Each curve has a 2-sol running mean applied for readability.

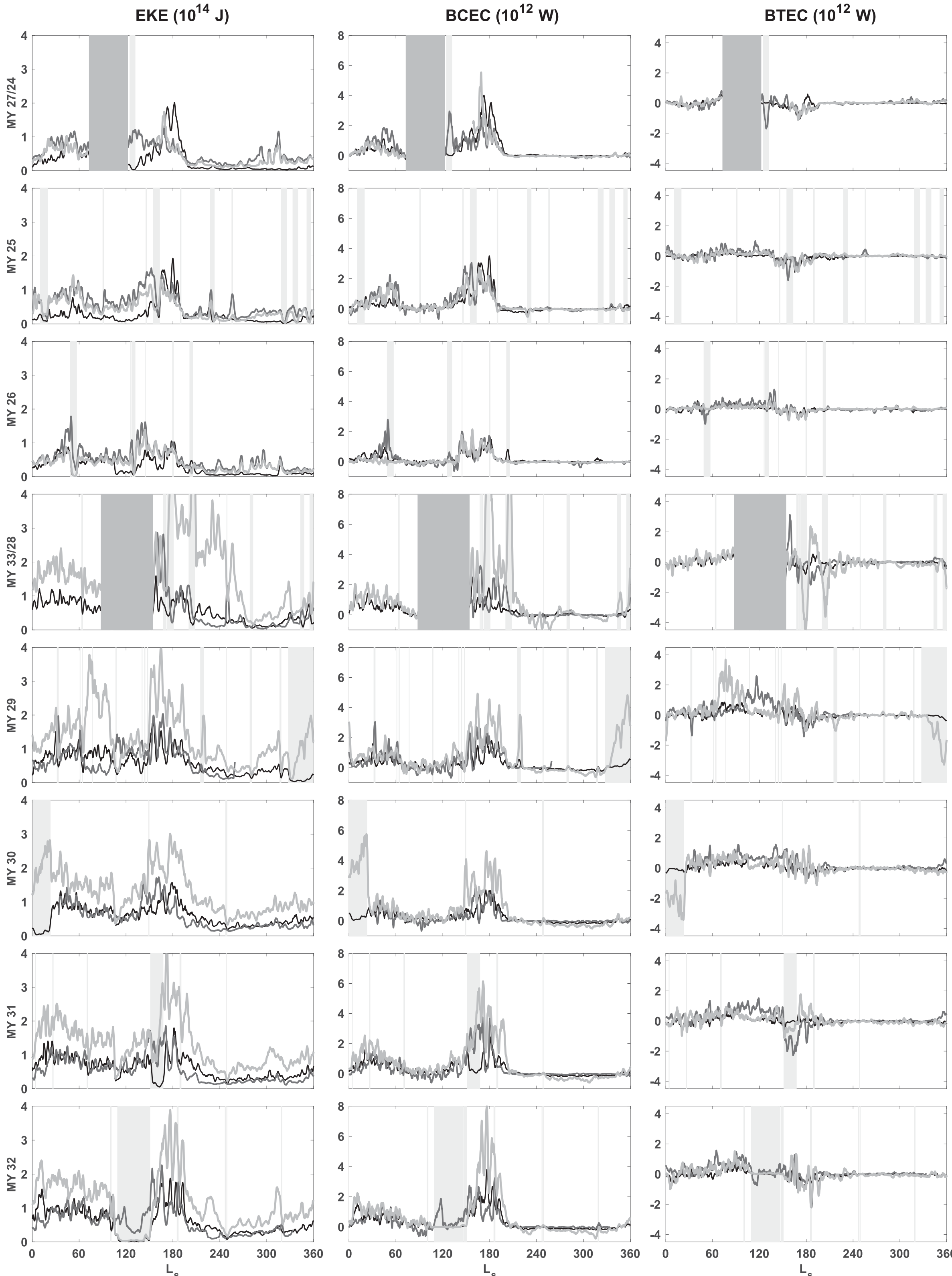

FIG. 2. As in Fig. 1, but for the latitude band 30°–90°S.

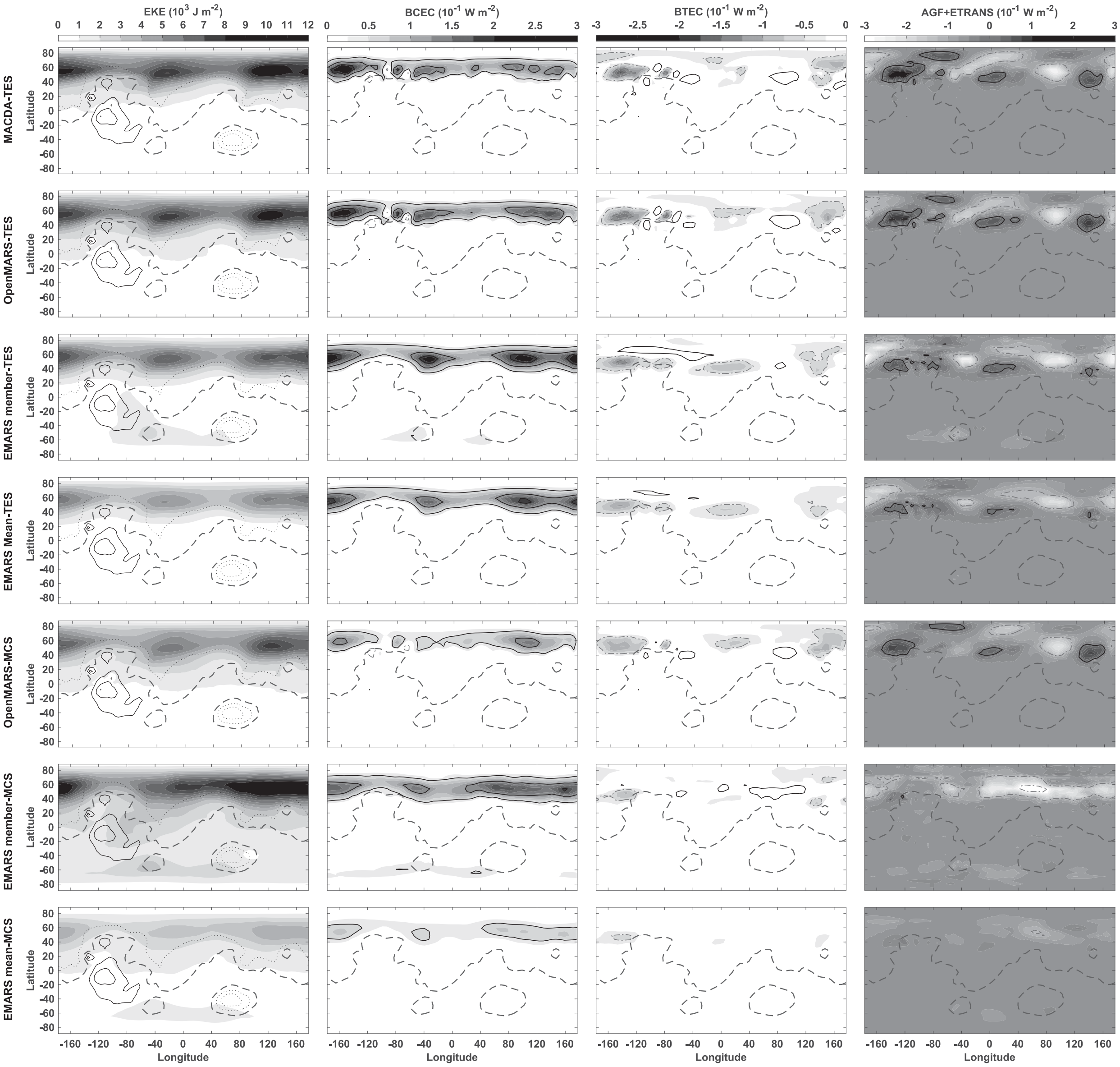

FIG. 3. Pressure-averaged EKE terms for the TES era for (first row) MACDA, (second row) OpenMARS, (third row) EMARS member, and (fourth row) EMARS ensemble mean and from the MCS era for (fifth row) OpenMARS, (sixth row) EMARS member, and (seventh row) EMARS ensemble mean. Averages are from the periods L_s = 190°–220° in MY 24, 26, and 29–32 and L_s = 330°–360° in MY 24, 26, and 30–32. Shown are (left) EKE, (left center) BCEC, (right center) BTEC + curvature, and (right) EKE flux convergence (AGF + ETRANS). Contours are every ±0.1 W m^{-2} starting at 0.05 for BCEC and BTEC and every ±0.2 W m^{-2} starting at 0.1 for AGF+ETRANS. Topography is shown in 3000-m increments in the left column, with negative values dotted and the 0 geoid dashed; only the 0 geoid is shown in the right three columns.

generated. The residual is primarily negative and somewhat smaller than the BTEC throughout all datasets (not shown), representing a frictional sink of EKE. When the surface drag term is included in the calculation of the residual for EMARS, the residual remains generally negative but becomes approximately one order of magnitude smaller than the energy conversion terms but still larger than the transport terms. Surface-pressure torques (Egger et al. 2007) are also part of the residual but have minimal contribution (<10^{-8} W m^{-2}) to the EKE budget due to the balance between eddy high and low pressure centers.

b. Integrated eddy kinetic energy equation terms

Based on the results presented in section 3a, the peaks of EKE, BCEC, and BTEC are selected and averaged in time and pressure to assess their spatial distribution. For the Northern Hemisphere (Fig. 3), two temporal ranges are averaged together: L_s = 190°–220° in MY 24, 26, and 29–32 and

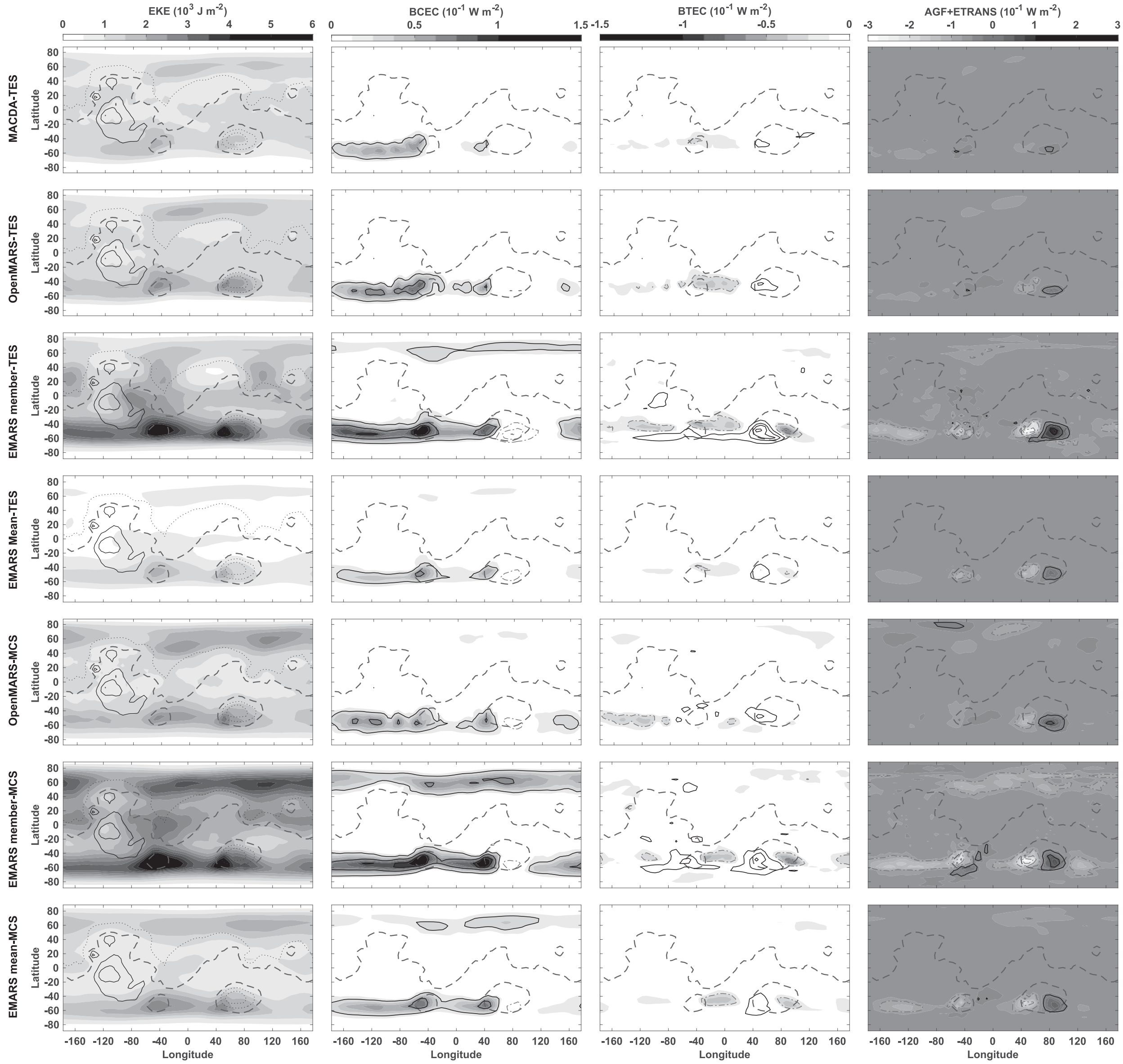

FIG. 4. As in Fig. 3, but averaged over the temporal ranges L_s = 30°–60° in MY 25–27, 29, and 31 and L_s = 150°–190° in MY 24, 26, and 29–32. Contours are every ±0.05 W m^{-2} starting at 0.025 for BCEC and BTEC and every ±0.1 W m^{-2} starting at 0.05 for AGF+ETRANS.

L_s = 330°–360° in MY 24, 26, and 30–32. For the Southern Hemisphere (Fig. 4), the averages are over L_s = 30°–60° in MY 25–27, 29, and 31 and L_s = 150°–190° in MY 24, 26, and 29–32. These ranges were selected in a two-step process: First, the EKE was summed across MY 24, 26, and 30–32 for MACDA, EMARS ensemble mean, and OpenMARS. Then times rounding to the nearest 10° of L_s were selected that contained the 90th percentile largest EKE.

The pressure-weighted, time-mean EKE terms are remarkably similar across datasets during both observational eras (Fig. 3), possibly because the storm tracks are constrained by topography (Hollingsworth et al. 1996). EKE (Fig. 3, first column) is greatest along 50°–60°N.

BCEC (Fig. 3, second column) is largest in Utopia Planitia, followed by Arcadia and Utopia (Table 1). The most negative BTEC is located just downstream of EKE maxima (Fig. 3, third column). The Reynolds stress is positive in regions of high topography (not shown) but when combined with the curvature and CFEI yields negative BTEC (section 4b). This implies that the short-period eddies can extract energy from the mean flow but lose it to other period eddies. The CFEI calculated for the exchange between the short-period eddies and the tides ($P <$

TABLE 1. Integrated time-average values of the EKE, BCEC, BTEC, AGF, and ETRANS for each Northern Hemisphere storm region between 30° and 90°N.

	Acidalia (275°–20°E)	Arcadia (150°–255°E)	Utopia (45°–150°E)
EKE (10^{13} J)	5.42	4.73	5.10
BCEC (10^{11} W)	3.53	2.89	3.04
BTEC (10^{11} W)	−0.34	−1.44	−0.11
AGF (10^{11} W)	−0.70	0.52	−0.10
ETRANS (10^{11} W)	0.25	−0.22	−0.34

1.5 sol) alone is approximately less than one-half of the interaction between the short-period eddies and long-period eddies ($8 < P < 60$ sol) shown here, so the loss of energy is primarily to the long-period eddies.

The EKE flux convergence (AGF + ETRANS) (Fig. 3, fourth column) exhibits a wavenumber-3 pattern at ~50°N. Generally, the negative regions are upstream of EKE centers along 50°N, and the positive centers are downstream. This is how the transport terms act in the aggregate sense on Earth as well: transporting energy from the upstream side of a given wave to the downstream side (Orlanski and Chang 1993). The exception to this mechanism is the transport in EMARS during the MCS era. The surface stress (only calculated for EMARS) is always negative and largest where the BCEC is largest (not shown); this indicates that friction acts to remove EKE in its primary generation locations.

Within each basin and in descending amplitude, both EKE and BCEC occur in Utopia (45°–150°E), Acidalia (275°–20°E), Utopia, and Arcadia (150°–255°E) Planitae, though there is EKE and BCEC across the entire zonal band (Table 1). BTEC, however, is over 4 times more negative in Arcadia than in either Acidalia or Utopia. Arcadia receives some of its positive EKE tendency from the EKE flux convergence, while EKE is lost from Acidalia and Utopia via EKE flux convergence. In totality, EKE generated in Acidalia and Utopia is transported to Arcadia where it is lost via BTEC, though the importance of this transport depends on the longitudes used to define the basins.

In the Southern Hemisphere, the behavior of the EKE terms broadly echoes that of the Northern Hemisphere but is impacted by the distinct southern topography. EKE is largest to the west of Argyre (~45°W) and Hellas (~70°E) basins, but there is a band of EKE to the south of Tharsis. Additionally, there is some overlap in the postsolstice periods for the Southern Hemisphere and the presolstice periods for the Northern Hemisphere; thus, there is some EKE in Acidalia and Utopia Planitae during these times. BCEC is maximized within the band to the south of Tharsis, which is similar to that found by Battalio et al. (2018b). BTEC has its largest negative values within and to the east of Argyre basin. There is a large positive region of BTEC on the western side of Hellas. Thus, EKE found near Hellas seems to be barotropically driven, but EKE to the west of Argyre is baroclinically driven. The baroclinic nature of the eddies near Solis Planitia and Argyre aligns with the Aonia–Solis–Valles Marineris dust storm track, which is generated by wave activity (Battalio and Wang 2019). The average EKE flux convergence consists of dipoles over Argyre and Hellas basins that are most pronounced during the MCS period. The negative poles are on the upstream side, and the positive poles are on the downstream side, operating in the same way as the EKE flux convergence in the Northern Hemisphere.

c. Zonal-mean energetics

The vertical distribution of energetics is shown in the zonal mean for the times defined in section 3b (Fig. 5). EKE is maximized between 100 and 1 Pa but extends to the surface between 40° and 80°N (Fig. 5), which aligns with previous findings (Greybush et al. 2013; Mooring and Wilson 2015; Battalio et al. 2016). There is a second region of EKE above 10 Pa from 50°N to the equator. While the EKE at the upper levels is generally larger in magnitude than that below 100 Pa, its relative contribution of the vertical average EKE value is reflected in the limited area encompassed with a linear pressure coordinate.

The vertical distribution of BCEC (Fig. 5, second column shading) matches the EKE; BCEC is positive between the surface and 10 Pa. BCEC aligns with the meridional transport of heat (Fig. 5, second column, contours) from the surface to 100 Pa and between 40° and 80°N. Eddies in this region are converting zonal potential energy to eddy potential energy via meridional eddy heat fluxes and from eddy potential energy to EKE via vertical heat fluxes.

BTEC is generally negative where BCEC is positive (Fig. 5, third column shading) due partly to the CFEI (Fig. 5, third column contours) but mostly due to curvature (not shown). The CFEI between the short-period eddies and the tides contributes to the positive BTEC near the surface and may be partly an artifact of using QG-ω (not shown). The negative regions of CFEI poleward of 60° represent the conversion of EKE from short-period to long-period eddies. These results match that of Wang et al. (2013) and Wang and Toigo (2016), as those energetics included the CFEI and curvature terms in the BTEC. The conversion from the mean flow to the eddies alone (not shown) is positive, matching Greybush et al. (2013) and Battalio et al. (2016). A region of positive BTEC and CFEI above 100 Pa between 40° and 60°N aligns with a negative region of BCEC and the secondary region of EKE, indicating that not all short-period waves are baroclinically driven.

EKE flux convergence redistributes the zonal-mean EKE. A region of negative EKE flux convergence occurs

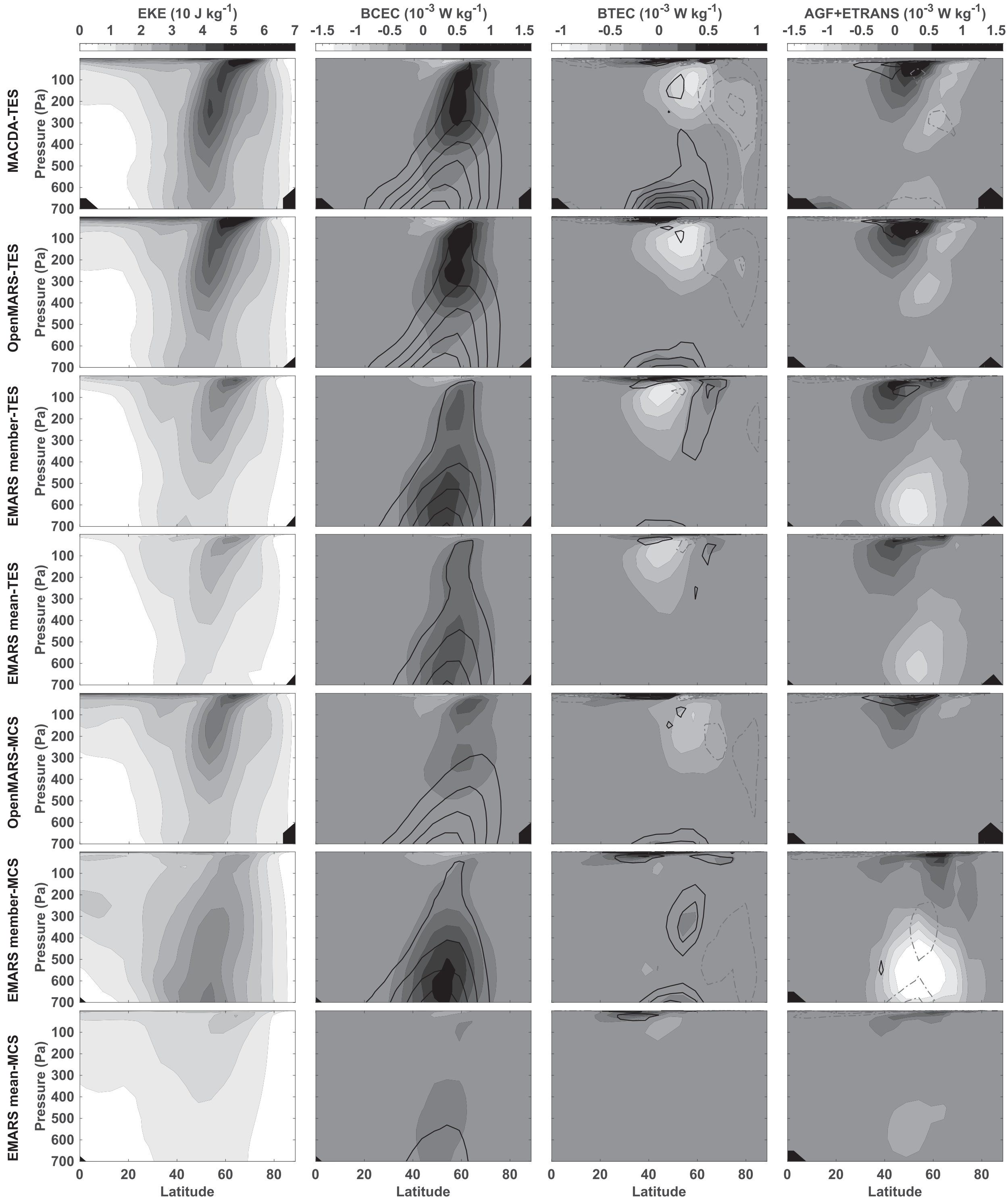

FIG. 5. Zonally averaged EKE terms for the same times as Fig. 3 for (first row) MACDA, (second row) OpenMARS, (third row) EMARS member, and (fourth row) EMARS mean from TES and for (fifth row) OpenMARS, (sixth row) EMARS member, and (seventh row) EMARS mean from MCS. Shown are (left) EKE, (left center) BCEC (shading) and meridional heat flux ($v'T'$, contoured every 5 K m s^{-1}), (right center) BTEC (shading) and CFEI (contoured every 10^{-4} W kg^{-1}), and (right) EKE flux convergence (AGF + ETRANS, shading) and ETRANS (contoured every 10^{-4} W kg^{-1}). Variables are weighted by cosψ. Black shading masks regions below the surface.

between 50° and 60°N that varies in height. It is between 400 and 100 Pa in MACDA and OpenMARS era but is near the surface in EMARS. Higher in the atmosphere, EKE flux convergence is positive in the TES era such that energy is removed between 50° and 70°N and deposited between 30° and 50°N, extending the storm track equatorward.

In the Southern Hemisphere, certain aspects of the eddy energetics are more complicated due to the large topography (Fig. 6). EKE peaks around 100 Pa in the midlatitudes only in the EMARS and OpenMARS-MCS datasets, which is similar to the Northern Hemisphere, but in MACDA and OpenMARS-TES, EKE is maximized above 10 Pa equatorward of 40°S (Fig. 6, first column). BCEC is broadly similar to that of the Northern Hemisphere, with a maximum between 40° and 70°S and 500–100 Pa and a negative region above (Fig. 6, second column, shading). Because of the Southern Hemisphere topography, BCEC is pushed higher in the atmosphere relative to the Northern Hemisphere. The reduced atmospheric column hinders the ability of eddies to efficiently transport heat (Battalio et al. 2018b).

BTEC is impacted by the topography to the greatest extent (Fig. 6, third column, shading). While there is a negative region of BTEC equatorward of each positive BCEC area, there are many other secondary maxima and minima near to the surface. This is because the topography is varied in the Southern Hemisphere, so the BTEC field is complex (Fig. 4), creating a noisy zonal mean. The EKE flux convergence is complex as well, but the main feature is the sink of EKE collocated with the positive BCEC in EMARS, similar to the Northern Hemisphere.

d. Eddy example during the MCS era

Specific case studies of eddy energetics have been investigated in the Northern (Battalio et al. 2016) and Southern Hemispheres (Battalio et al. 2018b) using MACDA, and the details for specific eddies are similar across datasets for the TES era generally (not shown). However, no cases from the MCS era have been described previously. A group of eddies that is robust across OpenMARS and the EMARS ensemble mean and member is selected using a Hovmöller of eddy surface pressure in MY 31 (Fig. 7). Whereas EMARS, MACDA, and OpenMARS agree well during the TES era (Fig. 16 of Greybush et al. 2019a), agreement between OpenMARS and EMARS is more rare during the MCS era due to lower sensitivity in the bottom few kilometers of the atmosphere from MCS (Greybush et al. 2019a). At some times, for example, L_s = 215°–220°, EMARS and OpenMARS do not even agree that coherent traveling waves are occurring. At other times, the wavenumber is different across datasets, causing waves to be 180° out of phase at some longitudes, for example, L_s = 190°–193° where OpenMARS has wavenumber 3 but EMARS has wavenumber 2. Nevertheless, for many other periods, there is reasonable agreement on wavenumber, relative amplitude, phase, and period of waves, including the period L_s = 203.0°–206.3°, which was the initiation time of the first major dust storm event of MY 31 (Kass et al. 2016; Battalio and Wang 2021).

Figure 8 shows the progression of eddy energetics during L_s = 203.0°–206.3°, MY 31 in comparison with the evolution of dust activity from the Mars Dust Activity Database (Battalio and Wang 2021). This period in MY 31 coincides with rapid dust area growth and flushing into the Southern Hemisphere. For this event, two flushing channels are activated, Acidalia and Utopia (Fig. 8, right column). Initially, EKE at L_s = 203.0° is also concentrated in Acidalia and Utopia, along with positive BCEC. Frontal dust storms are already ongoing at this initial time step. Over the following two sols (L_s = 203.5° and L_s = 204.1°), EKE and BCEC in Acidalia progress eastward toward Utopia, where BTEC becomes negative. As this occurs, a dust region in Acidalia passes north of Arabia Terra and into Utopia. From L_s = 204.6°, a new region of EKE develops in Acidalia via downstream development from AGF (not shown), which then subsequently grows baroclinically in the following two days (L_s = 205.2° and L_s = 205.8°), with some barotropic decay occurring on the last sol (L_s = 206.3°). Between L_s = 204.6° and L_s = 206.3°, a new dust event develops in Acidalia and flushes south with this eddy. Individual waves travel around the latitude circle as demonstrated in the continuous progression of eddy surface pressure behind frontal dust events (Fig. 8, column four, contours and Fig. 7), but both EMARS and OpenMARS pinpoint Utopia as a region of continuous EKE throughout the period. This is not a stationary wave, but instead eddy amplification occurs as waves pass through storm regions.

4. Discussion

a. Short-period eddy energetics on Mars

EKE for 1.5 < P < 8 sol eddies mainly occurs just before and after the solstitial pauses between 400 and 100 Pa along 50°N/S. EKE is amplified in the three Planitae in the Northern Hemisphere and in a band south of Tharsis and into Argyre basin. These storm tracks are not confined regions like they are on Earth but instead are regions where eddies achieve their maximum amplitude (Mooring and Wilson 2015). Generally, Utopia and Acidalia Planitae have the largest EKE, followed by Arcadia. Utopia Planitia has the largest BCEC, with Acidalia and Arcadia having somewhat less, though Arcadia has the largest-magnitude BTEC (Table 1). EKE is transferred across basins by the EKE flux convergence; EKE generated in Acidalia or Utopia by BCEC is transported to Arcadia where it is converted to the mean flow by BTEC (Table 1). However, despite the connection between transient waves and dust storms, the average amplitude of EKE does not necessarily indicate which dust storm track is the most productive at any given time, as Acidalia produces far more large dust events than Utopia and Arcadia combined (Battalio and Wang 2020, 2021). This indicates that wave amplitude is not the only factor in determining the locations of dust lifting.

Eddies on Mars convert energy from eddy potential energy to eddy kinetic energy via baroclinic instability. Eddy

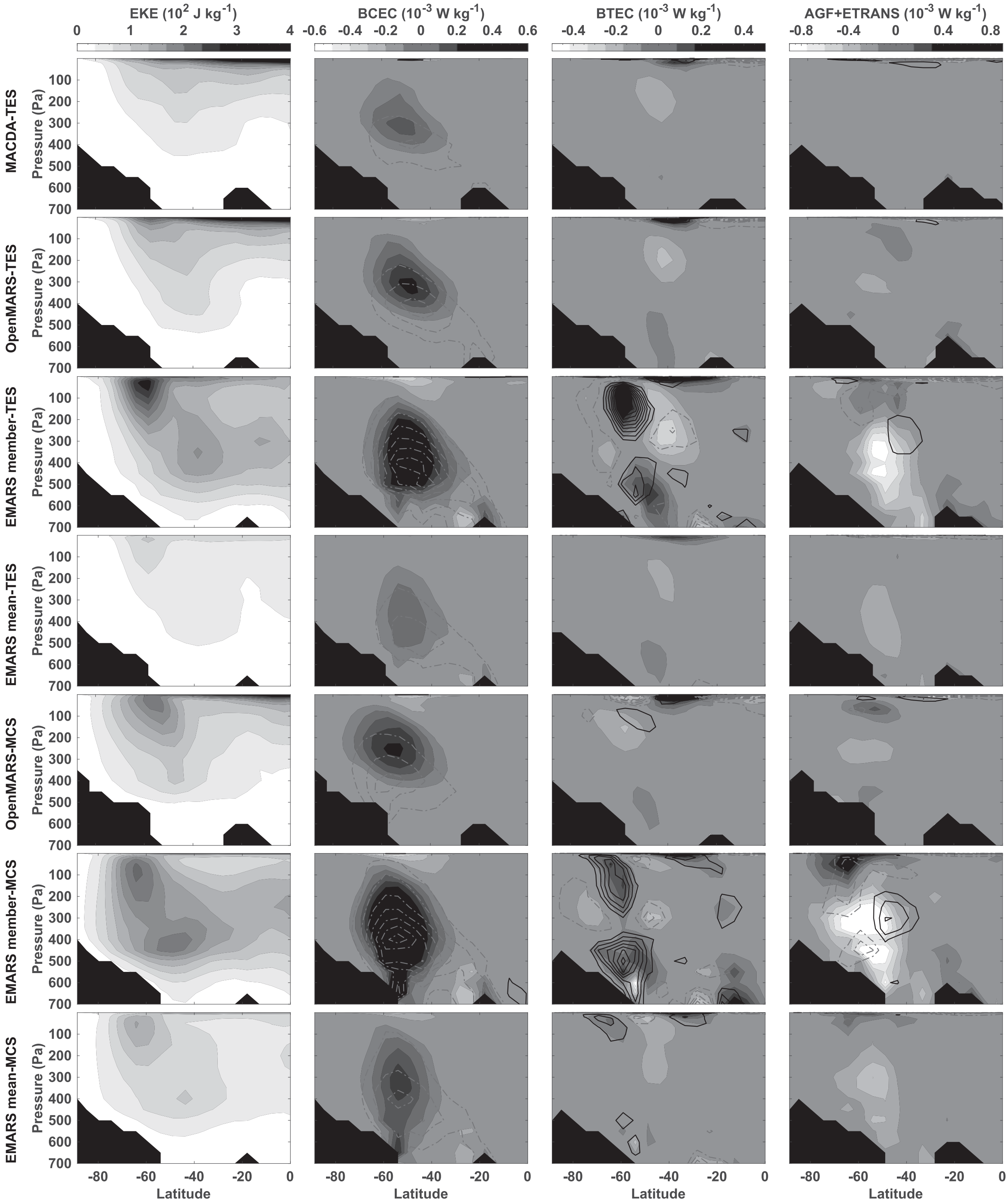

FIG. 6. As in Fig. 5, but for the Southern Hemisphere averaged over the time periods as Fig. 4.

generation predominantly occurs on the western side of the low topography Planitae, just upstream of EKE maxima. This is more apparent in the Northern Hemisphere eddies (Fig. 3) but also occurs in the Southern Hemisphere (Fig. 4). Vertically, BCEC occurs in the regions indicated by enhanced EKE, with the exception of EMARS-TES, which has surface

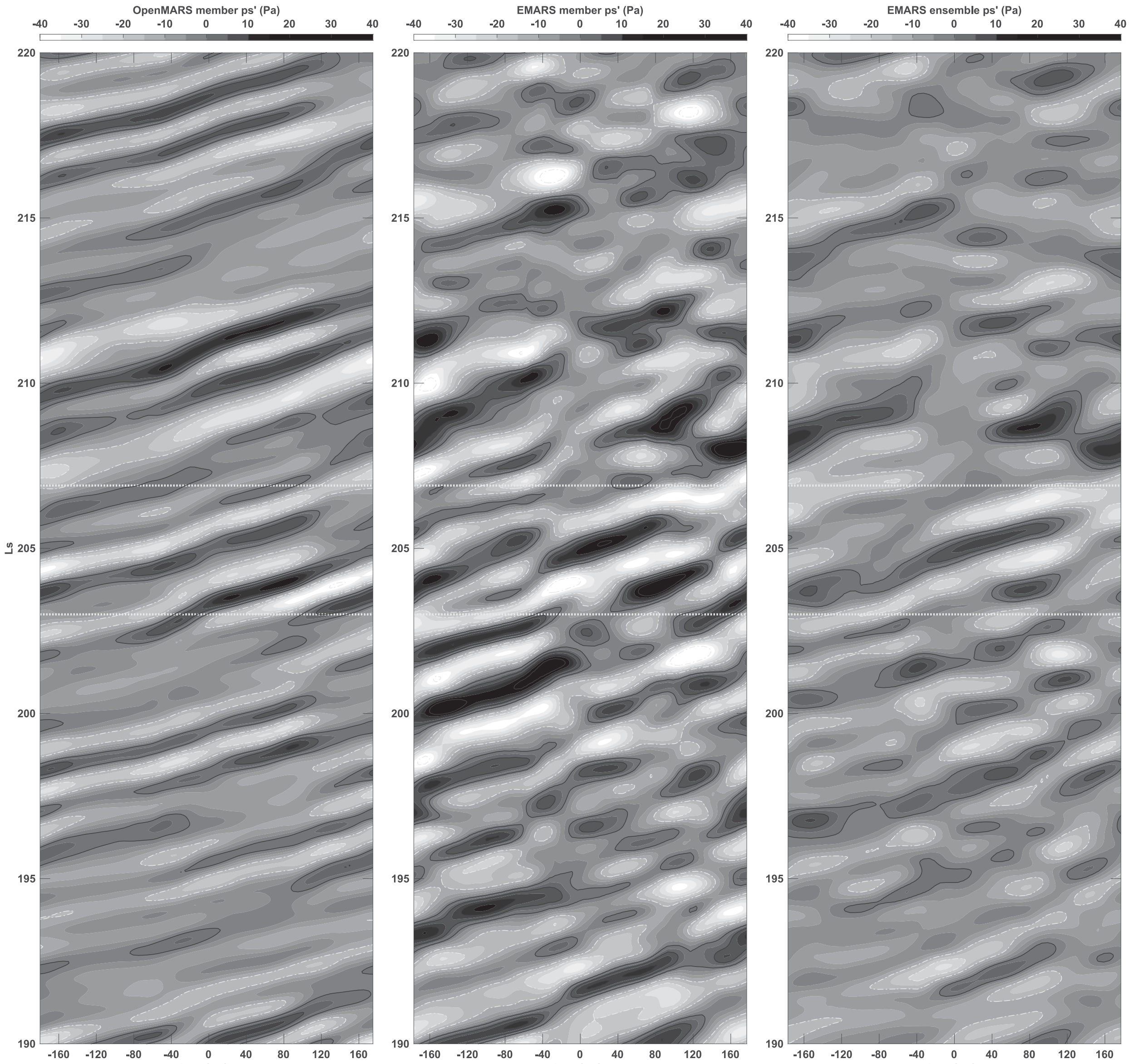

FIG. 7. Hovmöller diagram of eddy surface pressure from (left) OpenMARS, (center) EMARS member, and (right) EMARS ensemble mean for the period L_s = 190°–220° in MY 31, averaged over ~40°–80°N. Contours are every 10 Pa. Horizontal, gray dashed lines indicate the period shown in Fig. 8, below.

BCEC and upper-level EKE. These results agree with previous studies of eddy energetics for Mars (Greybush et al. 2013; Wang et al. 2013; Wang and Toigo 2016; Battalio et al. 2016, 2018b). There is also a small region of negative BCEC above 50 Pa poleward of ~40°N/S; here, eddies are converting energy from kinetic to eddy potential energy, which appears to be caused by barotropic forcing, perhaps as a result of the unstable annular polar vortex (Waugh et al. 2016).

The transport of EKE both by advection (ETRANS) and the pressure gradient force (AGF) plays a large role in shaping the storm tracks on Mars, though integrated over a hemisphere the transport is approximately zero (not shown). In the time mean across a hemisphere, EKE flux convergence moves EKE from the upstream side of the storm tracks where it is generated by BCEC to the downstream side where it is consumed by BTEC. This occurs within each Planitia in the Northern Hemisphere (Fig. 3, fourth column) and on either side of Hellas and Argyre basins in the Southern Hemisphere (Fig. 4, fourth column). In the vertical direction, EKE flux convergence redistributes EKE from the main BCEC generation area equatorward and upward (Figs. 5 and 6, fourth column).

One difference between baroclinic Rossby waves on Mars and Earth is that wave packets are not distinct entities on

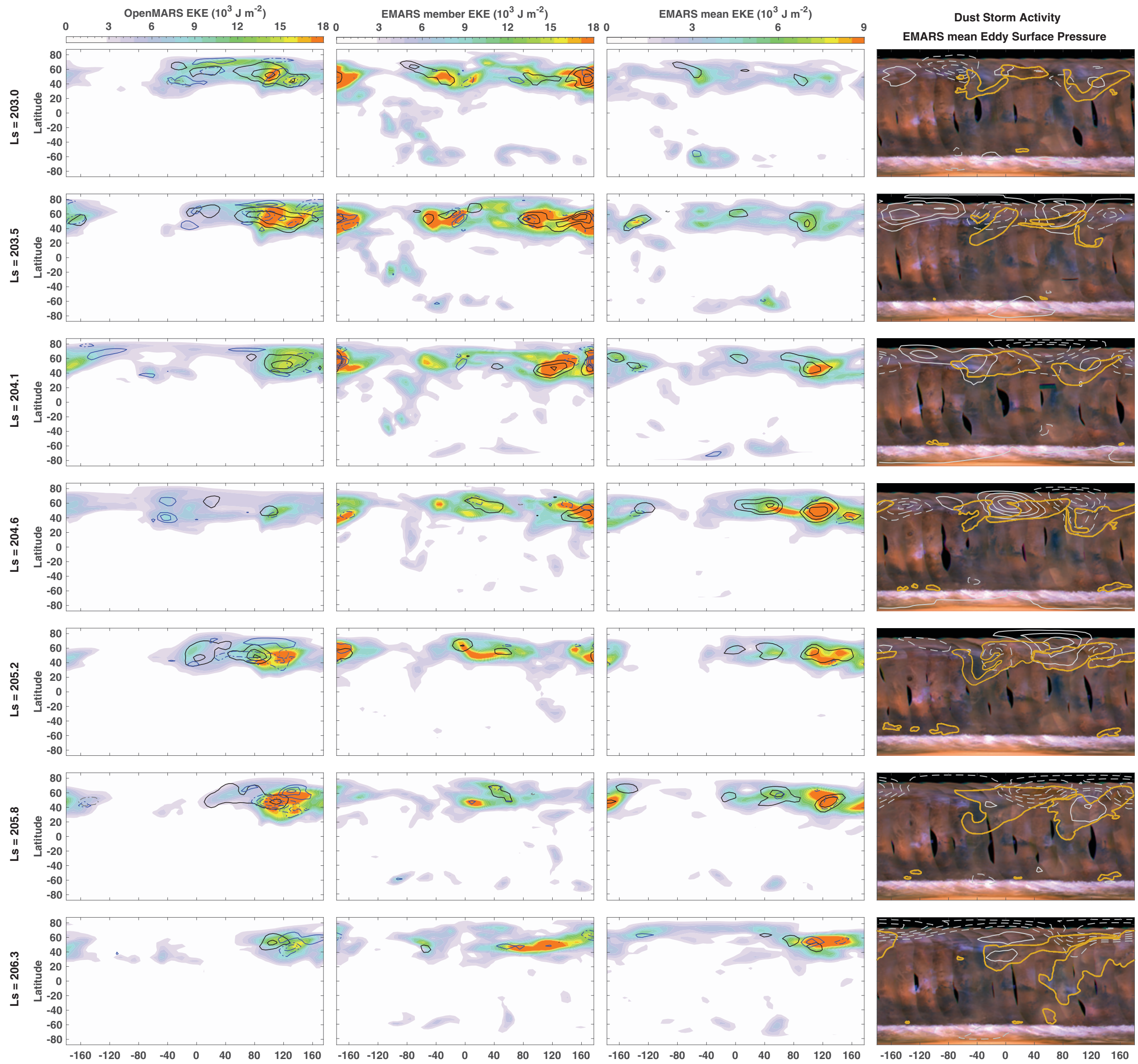

FIG. 8. Progression of a series of short-period eddies from MY 31 in (left) OpenMARS, (left center) EMARS member, and (right center) EMARS ensemble mean. In columns 1–3, vertically integrated EKE is shaded, and BCEC (black contours) and BTEC (blue contours) are contoured every 0.2 W m^{-2} for OpenMARS and EMARS ensemble mean and 0.4 W m^{-2} for EMARS member, with negative values dashed. Also shown are (right) Mars Daily Global Maps for each sol with outlines of dust activity from the Mars Dust Activity Database (Battalio and Wang 2021) shown in gold. Eddy surface pressure from the EMARS ensemble is contoured every 8 Pa, with negative values dashed. Each row is averaged for approximately 1 sol starting with the L_s listed at left and corresponding to the Mars Daily Global Maps.

Mars. On Earth, wave packets organize multiple individual eddies within a wave envelope that modulates the wave amplitudes (Lee and Held 1993). Downstream development of individual eddies occurs within wave packets (Chang 1993). Instead, on Mars, the individual waves are long relative to the planetary radius (zonal wavenumber 1–4 on Mars as compared with zonal wavenumber 5–8 on Earth) so that there is no separation between groups of waves. In other words, the wave packet encompasses the entire high latitudes when waves are amplified, and downstream development just refers to the transfer of energy from an upstream wave to a downstream wave.

b. Role of barotropic energy conversion

BTEC is a sink of energy for short-period waves. In the time mean, Northern Hemisphere BCEC and BTEC almost

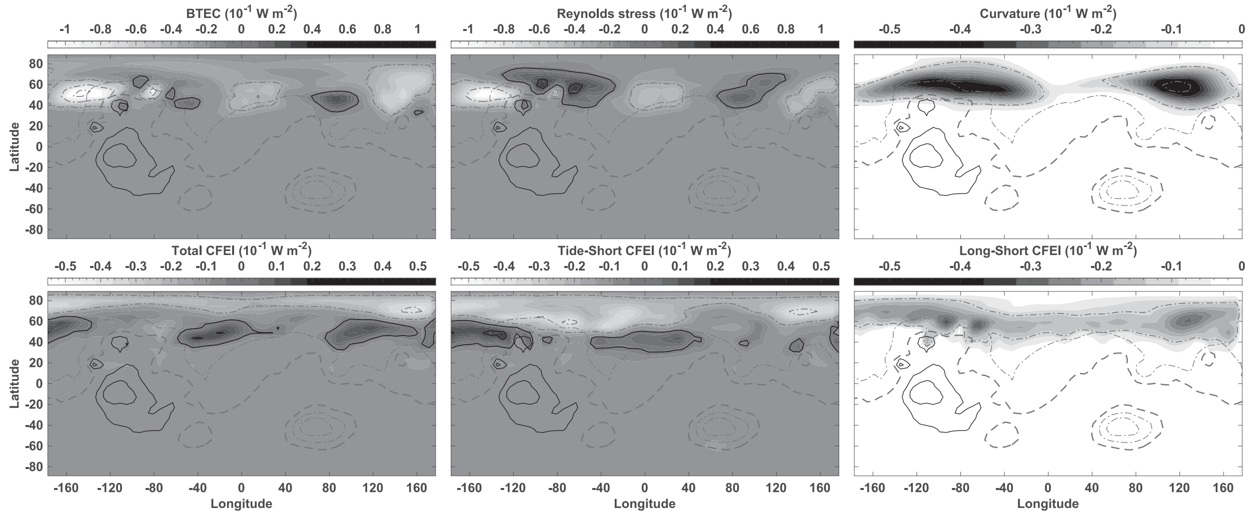

FIG. 9. Pressure-averaged (top left) total BTEC, (top center) Reynolds stress, and (top right) curvature and (bottom left) total CFEI, (bottom center) tide ($P < 1.1$) and short-period ($1.5 < P < 8$) CFEI, and (bottom right) long- ($8 < P < 60$) and short-period ($1.5 < P < 8$) CFEI. Averages are from the periods $L_s = 190°–220°$ in MY 24, 26, and 29–32 and $L_s = 330°–360°$ in MY 24, 26, and 30–32, with each individual period from MACDA, OpenMARS, and the EMARS ensemble mean weighted the same. Contours are every ± 0.05 W m^{-2} starting at 0.025 for BTEC and the Reynolds stress and every ± 0.025 W m^{-2} starting at 0.0125 for CFEI and curvature.

always oppose one another. Negative BTEC occurs on the eastern sides of the Planitae in the Northern Hemisphere (Fig. 3, third column) and on the eastern sides of Argyre and Hellas in the Southern Hemisphere (Fig. 4, third column). There are regions of positive BTEC on the northwestern sides of the Planitae and particularly on the western side of Hellas. BTEC is most strongly negative from roughly 40° to 80°N and 600 to 10 Pa and positive from 20° to 80°N between 100 and 0.1 Pa and below 600 Pa (Fig. 5, third column).

Wang et al. (2013) and Wang and Toigo (2016) define BTEC as exchange between the mean flow and eddies (Reynolds stresses) plus conversion between eddies of various periods (CFEI) plus effects induced by the curvature of the planet. Battalio et al. (2016) and others define the BTEC as essentially the Reynolds stresses alone, and eddies are lumped together regardless of period, with only the tides excluded. By including all eddies, there can be no interactions between eddies of different periods, and the CFEI term averages to zero. To ameliorate these issues, three improvements have been implemented here to the local energetics analysis of BTEC. First, the range of eddy periods is confined to $1.5 < P < 8$ sols, corresponding to the specific periods of the transient waves of interest, meaning that short-period eddies can lose energy to long-period eddies or the tides. Second, an improved filtering method for the CFEI is used (Jiang et al. 2013) that better measures eddy–eddy interactions by filtering over the eddy periods and not taking the time mean. Last, the curvature term is explicitly calculated.

As presented in section 3b, BTEC is negative when defined as Reynolds stress + CFEI + curvature in the Northern Hemisphere (Fig. 9) and in the Southern Hemisphere (not shown). Energy exchange between the mean flow and the eddies depends on the location relative to topographic features. EKE is converted from the eddies to the mean flow (negative BTEC) when the flow interacts with high relief (Fig. 9, second column, top). The curvature term is negligible for local energetics analyses of Earth (McLay and Martin 2002); however, for Mars, curvature plays an important role in balancing the short-period eddy energetics by being a sink of EKE in the locations where the Reynolds stresses are positive (Fig. 9, middle column, top). CFEI between the short- and long ($8 < P < 60$)-period eddies is a sink of short-period EKE within the three main storm tracks and is not a source of short-period EKE in any region, meaning short-period eddies always pass energy to long-period waves (Fig. 9, right column, bottom). However, positive CFEI between the tides ($P < 1.5$) and short-period eddies indicates a gain of short-period EKE from the tides within the northern basins along 40°N, with negative tide-short CFEI along 60°–80°N (Fig. 9, middle column, bottom). The total CFEI results in a loss of EKE from the short-period eddies (Fig. 9, left column, bottom). In the zonal mean, the CFEI and curvature terms are the primary sinks of EKE in the regions of greatest BCEC. Indeed, an analysis of $8 < P < 30$ sol eddies finds that the total BTEC and CFEI for these long-period eddies is positive and somewhat larger magnitude than that of short-period eddies, meaning the long-period eddies gain EKE barotropically. More importantly, long-period eddies extract EKE from the short-period eddies (not shown). This rectifies work showing that in the global mean and for all eddies with $P < 30$, BTEC is a small source of energy (Tabataba-Vakili et al. 2015).

c. *Altered energetics of the solstitial pause*

Waves during the solstitial pause are different in amplitude, wavenumber, and the height above the surface (Lewis et al. 2016). Subsequently, the eddy energetics of these waves substantially differs from those occurring in fall and late winter;

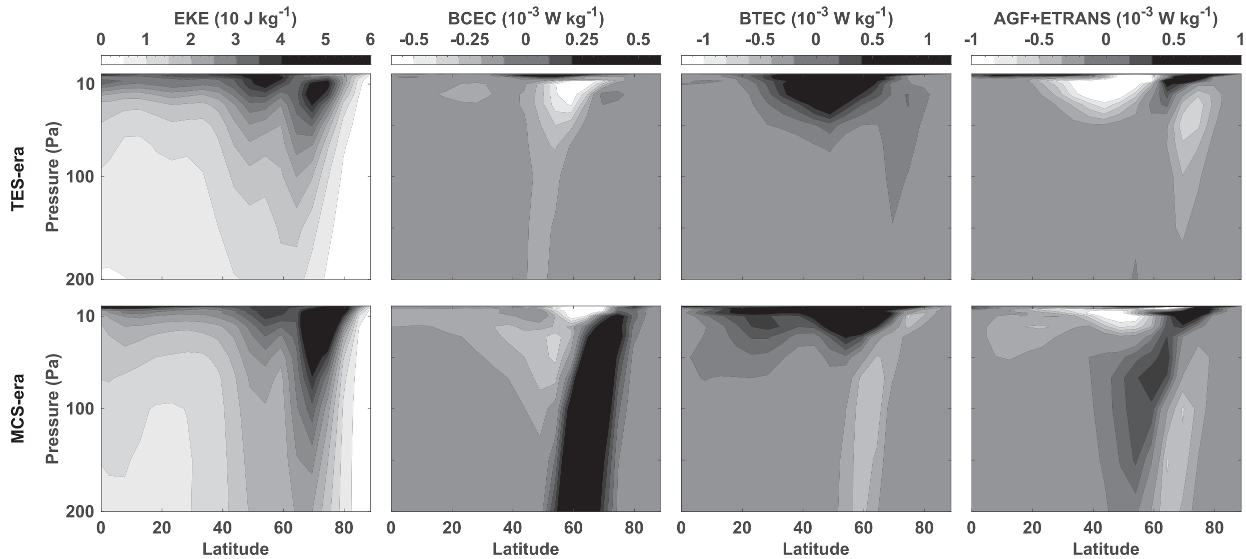

FIG. 10. Zonally averaged EKE terms but averaged across MACDA, OpenMARS, and EMARS ensemble mean for both (top) TES and (bottom) MCS eras for L_s = 260°–290° in MY 24 and 26 in the TES era and MY 29, 30, 31, and 32 in the MCS era. Shown are (left) EKE, (left center) BCEC, (right center) BTEC, and (right) EKE flux convergence (AGF + ETRANS). Variables are weighted by cosψ.

however, there are clear discrepancies between the results of the MCS and TES eras. MCS-era eddies during the solstitial pause in OpenMARS and the EMARS ensemble member are not dramatically different from those during fall or late winter (Fig. 10, bottom row), which is attributable to poor observational constraints on the lower atmosphere. This points toward an inability of the MGCMs underlying EMARS and OpenMARS to capture the solstitial pause without being forced by observations. Indeed, the energetics in the EMARS-MCS ensemble mean more resembles those from the TES era due to the lack of agreement among EMARS members during the MCS era (not shown), which leads to a weakened ensemble mean. It is also possible that individual EMARS ensemble members, which vary across water cloud particle and dust particle properties (section 2a), may have sufficiently large pauses to impact the ensemble mean, because increased dust or water ice cloud opacity can produce a pause in MGCMs (Mulholland et al. 2016; Lee et al. 2018).

Focusing on the Northern Hemisphere, EKE is confined above 30 Pa between 40° and 60°N during the TES era (Fig. 10, top row). Some EKE extends toward the surface but not nearly to the same degree as during the most active transient wave seasons (Fig. 10, first column). Positive BCEC is essentially absent during this time, and there are regions of negative BCEC collocated with EKE (Fig. 10, second column). Instead, the source of EKE during this time is BTEC, which partly comes from CFEI, but the majority of eddy energy is extracted from the mean flow itself (Fig. 10, third column). At pressures higher than 200 Pa, little BTEC or energy transport is found. Together, these suggest that the character of eddies during the pause is fundamentally different than that of eddies found near the surface in fall and late winter.

Eddies during the solstitial pause are not baroclinic but not necessarily because the environment is not favorable for baroclinic instability. The proclivity for baroclinic instability is quantified using the baroclinic parameter or Eady index:

$$\sigma = 0.31f\left(\frac{\partial u}{\partial z}\right)(N)^{-1}, \tag{2}$$

where N is the Brunt–Väisälä frequency, f is the Coriolis parameter, and u is the zonal wind component. Mulholland et al. (2016) hypothesized that the solstitial pause was created in part due to the impact of clouds and dust on the temperature gradients, a finding replicated by Lee et al. (2018). Polar warming decreases meridional temperature gradients and by thermal wind balance reduces the vertical wind shear (Kuroda et al. 2007). A similar increase in stability occurs during GDEs (Battalio et al. 2016). Though the correlation between eddy intensity and the Eady index holds for multiple MGCMs at specific levels, the relationship is not as robust for the reanalyses themselves (Mulholland et al. 2016; Mooring et al. 2019). The baroclinicity does decrease during the solstitial pause each year below 200 Pa (Fig. 11, shading), mostly due to decreased N^{-1} rather than a change in wind shear (not shown), because of this, the BCEC should change in proportion to the Eady index. However, the integrated Eady index does not decrease enough during the TES era to account for the drastic reduction in BCEC, which approaches zero during solstice during the TES era (Fig. 11, contours and Fig. 1).

Solstitial reductions in baroclinic activity appear to be an intrinsic quality of terrestrial storm tracks (Novak et al. 2020), and Earth's northern Pacific track has a pause in eddy activity despite baroclinicity peaking at solstice (Nakamura 1992). This indicates that the dramatic decrease in eddy activity during the Martian pause may be due to fundamental storm track

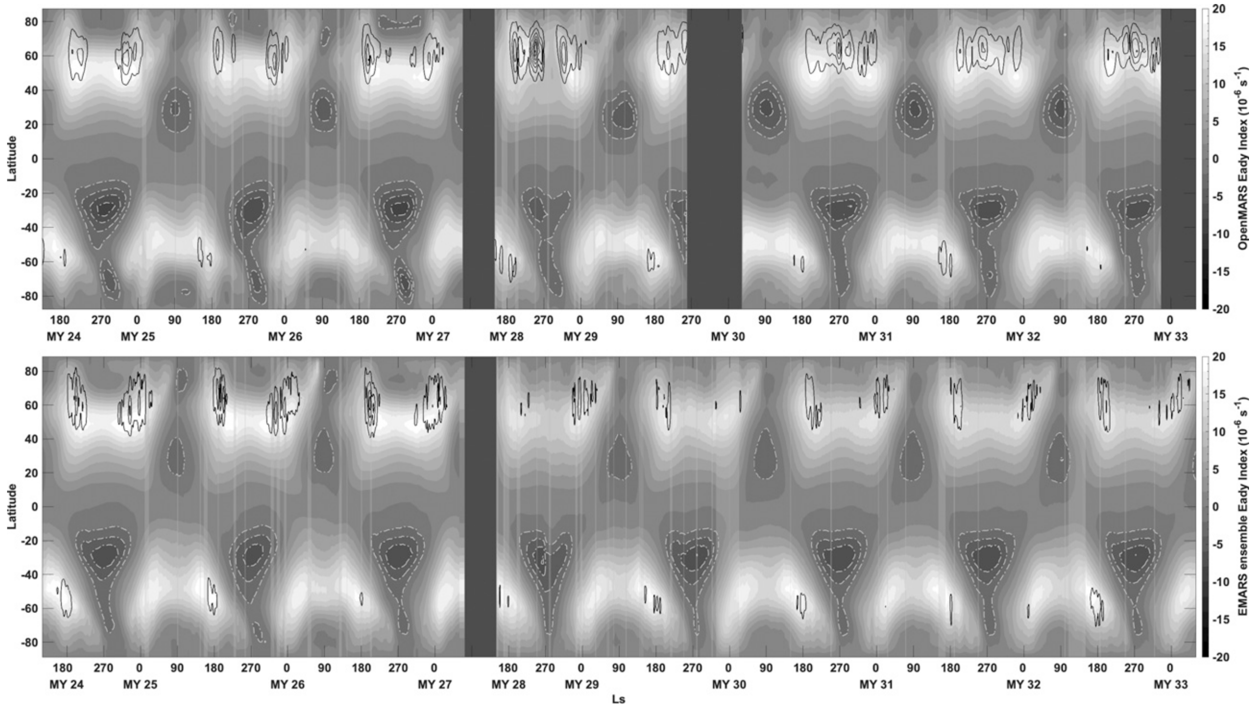

FIG. 11. Evolution of the zonally and vertically integrated (from surface to 200 Pa) Eady index for (top) OpenMARS and the (bottom) EMARS ensemble mean. Negative values are indicated with dot–dashed contours every 2×10^{-6} s^{-1}. The vertically integrated BCEC is contoured every 2 W m^{-2} starting at 1 W m^{-2} in solid black lines. Gaps in the dataset are covered in dark gray, and periods lacking assimilated observations are indicated with light gray bars.

dynamics acting in combination with the unique conditions of Mars, (e.g., dust loading, clouds, and CO_2 deposition). Further, the barotropic character of waves in the upper levels (Fig. 10) indicates that linear baroclinic instability theory will not inform the growth mechanisms of these waves, which instead may be a response to the barotropically unstable annular polar vortex at these heights (Waugh et al. 2016; Toigo et al. 2017; Seviour et al. 2017).

During the MCS era and particularly during MY 31–33, OpenMARS has a peak in baroclinicity at solstice displaced poleward from the surrounding seasonal nature of the waves (Fig. 11, top), and BCEC peaks within this region. This problem is not echoed in the EMARS ensemble mean (Fig. 11, bottom) but does occur in the single EMARS member (not shown). Instead, baroclinicity is reduced at solstice in the Northern Hemisphere in the EMARS ensemble, which partly accounts for the reduced BCEC found during these years (Fig. 5). Again, the reanalyses struggle in resolving eddies at the lower levels during the MCS era. Either the MGCMs underlying the reanalyses are missing some aspect of the real Martian atmosphere that causes the pause or are not correctly representing the storm track dynamics that contribute to eddy reduction at solstice. Additional investigation of the dynamical cause of the Martian solstitial pause in light of more recent advances in terrestrial theory (e.g., Novak et al. 2020) is warranted.

d. *Differences across reanalyses*

The reanalyses closely agree during the TES era, with individual peaks in EKE aligning across all reanalyses in the Northern Hemisphere (Fig. 1) and the Southern Hemisphere (Fig. 2). However, there are rare instances where one reanalysis is an outlier, for example, in the Southern Hemisphere during MY 24 around $L_s = 180°$, when the EMARS ensemble mean exhibits a peak not occurring in either MACDA or OpenMARS. Within the MCS era, there can be great disparities in the representation of eddies between datasets where individual peaks do not align, but the overall seasonal and annual trends in activity are broadly similar. EKE is more amplified in the EMARS member across the MCS era in both hemispheres, but the EMARS ensemble mean has amplitudes comparable to the deterministic OpenMARS and MACDA across the entire duration of analysis in the Southern Hemisphere (Fig. 2). In the Northern Hemisphere for the MCS era, the EMARS ensemble mean has smaller amplitude EKE equation terms than either MACDA or OpenMARS during the transient eddy season of $L_s = 180°$–$30°$ (Fig. 1). The EMARS member (Fig. 2, light gray, MY 28–33) has much higher amplitudes for EKE and BCEC across almost all MCS years in both hemispheres, nearly double the ensemble mean value. During the MCS era, OpenMARS results match more closely in amplitude and timing with the EMARS member in the Northern Hemisphere but with the ensemble mean in the Southern Hemisphere. The reason the EMARS ensemble mean better matches the deterministic OpenMARS for the Southern Hemisphere is not clear. In this way, the EMARS ensemble is a distinct improvement over viewing a single EMARS member, as the single member appears to be an outlier for larger-eddy energetics amplitudes.

The largest differences between datasets occur when the models underlying the reanalyses are not constrained by observations, regardless of observation era. The decline and improvement of reanalysis data is a well-known issue for terrestrial datasets, but the issues found in terrestrial reanalyses are mollified by the amount of data assimilated and by the increasing quality of observations (Diniz and Todling 2020). However, for Mars, the issue is apparent given that the total number of observations at a given time step relies on a single instrument. Both MGCMs have a tendency to amplify eddies when unconstrained by observations. The stochastic growth of eddies causes different periods and wavenumbers to grow in the individual ensemble members, reducing the eddy activity in the EMARS ensemble mean. This is evident in years where eddies in the Northern Hemisphere are favored but there are periods of no observations, especially L_s = 320°–360° in MY 25. In each of three observation gaps, the integrated EKE immediately drops in the EMARS ensemble (Fig. 1) but quickly increases in MACDA, OpenMARS, and the EMARS member. This is also true earlier in MY 25 around L_s = 220°, a time when eddies are less favored due to the conditions of the MY 25 GDE (Battalio et al. 2016). Thus, for sufficiently long gaps in observations, each of these datasets rapidly reverts to free-running MGCM simulations and cannot be relied upon for comparison with reality.

The time-mean spatial distribution of eddies reasonably agrees across reanalyses (Fig. 3). However, the exact locations of BCEC maxima are not as well aligned across datasets as EKE. For the EMARS ensemble mean, BCEC maxima are located upstream of their respective EKE maxima, but this is not necessarily true for the maxima associated with the Utopia and Arcadia EKE regions in MACDA and OpenMARS. Further, there are more individual, local maxima in the MACDA and OpenMARS reanalyses. The less smooth BCEC in these datasets may be the result of their deterministic nature, as opposed to the smoothing character of an ensemble average, and the impact of QG-ω versus a model-provided ω (Battalio and Dyer 2017). In the Southern Hemisphere, the storm region between Argyre and Hellas basins is reduced in MACDA relative to other datasets (Fig. 4). Similarly, the vertical distribution of eddies varies across reanalyses. BCEC and AGF in OpenMARS and MACDA occur most strongly between 400 and 100 Pa, while in EMARS, BCEC and AGF occur predominantly at the surface (Figs. 5 and 6). The opposite is true for the BTEC, which is positive at the surface in OpenMARS and MACDA. These differences are partly attributable to the use of QG-ω in the OpenMARS and MACDA analyses and the model-provided ω for EMARS. Because ω' from QG-ω vanishes at the surface, so too does BCEC for the OpenMARS and MACDA. When calculating BCEC using QG-ω for EMARS, the maximum of BCEC shifts upward as well (not shown). Consequently, the EMARS member has BCEC—and therefore EKE—much closer to the surface.

The specific details of individual waves show good agreement during the TES era, but during the MCS era, there are periods where the individual datasets disagree on wavenumber, period, and amplitude (Fig. 7). However, for many periods, the datasets synchronize on wave characteristics. During a major MY 31 dust event around L_s = 203°, the reanalyses pinpoint the dust growth regions of Acidalia and Utopia for large EKE and BCEC. EKE is largest in the EMARS member and smallest in the EMARS ensemble mean (Fig. 8; note the different color scales in each column). Baroclinic growth and barotropic decay of the regions of EKE are most cleanly shown in the EMARS ensemble mean and OpenMARS; however, the deterministic OpenMARS and EMARS member have considerably more noise than the EMARS ensemble mean. While the overall regions of EKE and energy conversion agree during this time, there are some time steps where the single EMARS member and mean have considerable disagreement on the details of the eddy energetics. At L_s = 205.2°, the largest amplitude EKE is found in Acidalia in the EMARS member, with little EKE in Utopia, but the EMARS mean has the reverse of that. For this case, the EMARS mean agrees better with OpenMARS than its own member. This demonstrates the usefulness of an ensemble dataset in diagnosing specific events. The agreement of OpenMARS and the EMARS ensemble mean with observed dust activity opens the possibility of storm diagnosis using eddy energetics, wave activity, or potential vorticity analysis. Detailed analysis of each of the major dust events in the MDAD using OpenMARS and EMARS will be the subject of future work.

e. *Differences between observational eras*

MCS observations are known to poorly constrain eddies in the lowest scale height due to limited sensitivity in the bottom few kilometers of the atmosphere (Greybush et al. 2019a) and due to limited coverage during times of high opacity (Shirley et al. 2015). The result is that eddy energetics during the MCS period is not as consistent across reanalyses as during the TES period. EKE amplitude jumps considerably in the EMARS member from the TES to MCS eras (not shown) and shifts toward the surface (Figs. 5 and 6).

Poor coverage in the lowest scale height by MCS impacts the representation of the solstitial pause. In the TES years, solstitial reduction of eddies is clear in MYs 24–26 (section 4c). In the MCS years, the solstitial pause is muted (Fig. 1, left column) by a reduction of wave energy in fall and late winter and by a lack of a reduction during midwinter in comparison with TES years, leading to near-constant eddy activity during L_s = 180°–360°. The problem is compounded in OpenMARS, where eddy activity peaks at winter solstice (Fig. 1, left column). This eddy activity is due to large BCEC in midwinter (Figs. 1 and 11). Observations and MGCM simulations of the pause indicate that wavenumber 3 is the most impacted (Banfield et al. 2004; Wang and Toigo 2016; Greybush et al.

2019a). Given the location of wavenumber 3 in the lowest levels (Wang and Toigo 2016; Greybush et al. 2019a), wavenumber 3 is most impacted by the reduction in quality of observations of the lowest levels of the atmosphere during the MCS era. Rogberg et al. (2010) showed that the internal chaotic growth of baroclinic transients resulted in divergence between free-running model forecasts and observation-constrained simulations on time scales <10 sols. The very short dynamical time scale on Mars leads to the divergence of the EMARS ensemble, as indicated by the much lower ensemble-mean energetics during the MCS era than the single member (Greybush et al. 2019a). While the Northern Hemisphere does not have a solstitial pause during the MCS era, the Southern Hemisphere does. This may be due to the Southern Hemisphere surface being higher and therefore in the region better constrained by MCS (Battalio et al. 2018b). Despite the difficulty with which MCS observations constrain the lowest scale height, they significantly improve the representation of low-level eddies relative to free-running simulations. For example, during a observation gap between $L_s = 320°$, MY 29 and $L_s = 25°$, MY 30, EKE drops to less than a quarter of the climatological value in the EMARS mean, but EKE in the EMARS member rapidly increases, indicating a lack of ensemble agreement.

Future studies using EMARS and OpenMARS to diagnose specific transient eddies events must use caution during the MCS era. Many periods of eddy activity do not agree on phase, wavenumber, wave amplitude, and wave period from OpenMARS to EMARS (Fig. 7). Within the EMARS ensemble, many periods where regular traveling waves should be expected to exist exhibit little coherent behavior in wave activity, for example, after $L_s = 190°$ in MY 31 (Fig. 7, right column). However, higher confidence is warranted when the EMARS ensemble agrees with its member and OpenMARS and with the locations of observed dust activity, for example, during the window of $L_s = 203°$–$207°$ in MY 31 (Fig. 8). That two separate reanalyses agree on the broad placement of wave structures in the context of visible frontal dust systems as seen in the independently collected Mars Dust Activity Database (Battalio and Wang 2021) increases the overall confidence in the accuracy of each dataset.

5. Conclusions

The local eddy energetics diagnostic paradigm is used to compare short-period ($1.5 < P < 8$ sol) transient eddies across 8 Mars years. The dynamics of these eddies is compared across two observational eras and three Martian reanalysis datasets: MACDA, EMARS, and OpenMARS. Further, within this framework, previous conflicting results on the nature of Martian transient waves are unified. The overall time-mean structure of the eddies is similar, but the time-mean eddy activity is larger when observations are available from the Thermal Emission Spectrometer (TES; Mars years 24–27) versus from the Mars Climate Sounder (MCS; MY 28–33) due to near-surface eddies being less constrained by MCS temperature retrievals. Eddy kinetic energy is maximized in three tracks in Utopia, Arcadia, and Acidalia Planitae between 40° and 70°N (Fig. 3) and upstream of Hellas and Argyre basins between 40° and 70°S (Fig. 4). Eddies are not limited to specific longitudinal regions but amplify as they traverse each (Fig. 7) (Mooring and Wilson 2015). Eddies in the Northern Hemisphere are considerably stronger than the Southern Hemisphere.

Baroclinic energy conversion is the primary source of eddy kinetic energy in the midlatitudes in the lowland Planitae in the Northern Hemisphere and to the west of Hellas and Argyre basins in the Southern Hemisphere. Barotropic energy conversion serves as the main sink of eddy kinetic energy due to a combination of planetary curvature and loss to longer-period eddies. Interactions with high topography cause eddies to extract energy from the mean flow; elsewhere, eddies lose energy to the mean flow. For each hemisphere, eddies are amplified in fall and late winter, with a reduction of eddy activity in between (Figs. 1 and 2). The pause in activity may in part be due to dust and clouds impacting temperature gradients (Mulholland et al. 2016), but the reduction in potential eddy growth rate is not as pronounced as the reduction in realized baroclinic energy conversion (Fig. 11), indicating that internal dynamics may be important.

Although the characteristics of specific times of eddy activity agree well across reanalyses during the TES observational era (Greybush et al. 2019b), the characteristics of specific times of eddy activity can vary greatly across reanalyses during the MCS era (Fig. 7). However, when the reanalyses are in agreement, the locations of eddy kinetic energy and baroclinic and barotropic energy conversions favorably align with locations of large dust storm activity from the Mars Dust Activity Database (Battalio and Wang 2021). Downstream development through ageostrophic geopotential flux convergence drives eddy growth until baroclinic energy conversion increases. As this occurs on the upstream side of the three northern storm regions, dust lifting begins with advection carrying dust east and occasionally south. As eddies exit the Planitae, barotropic energy conversion removes eddy kinetic energy, and ageostrophic geopotential flux divergence extracts energy and deposits it downstream for subsequent eddy development. This process broadly aligns with development of terrestrial eddies (e.g., Orlanski and Katzfey 1991) and previous analyses for Mars (e.g., Battalio et al. 2016).

In comparison with the energetics presented in Battalio et al. (2016) from MACDA, regions of large-eddy kinetic energy and energy conversion for specific events are less discrete and are instead spread over a wider longitudinal region (Fig. 8). While this might be due to interseasonal and interannual variability, much of the difference stems from difficulties in the datasets for resolving eddies in the MCS era. Because of the poor match between reanalyses for some times, caution should be used in diagnosing near-surface traveling eddies or comparing dust storm evolution with individual eddies in only one reanalysis; however, there is considerably more agreement between reanalyses and within the EMARS ensemble when observations are available versus when the simulations are free-running, even during the MCS era. Because there are times of poor agreement between reanalyses and within the

EMARS ensemble during the MCS era, additional observational platforms in the form of surface stations networks, areostationary satellite constellations, or additional polar-orbiting satellites will be required to improve the quality of these reanalyses. More specifically, instrument design should focus on observing the lower-scale heights of the Martian atmosphere, though assimilation of new MCS products may provide additional constraints on low-level eddies (Hinson and Wilson 2021).

The results presented here unify conflicts between previous work for Mars about the nature of barotropic energy conversion (BTEC). Some results point to positive conversion, whereupon short-period eddies gain energy barotropically (Tabataba-Vakili et al. 2015; Greybush et al. 2013; Battalio et al. 2016, 2018b,a), but other work suggests the opposite (Wang et al. 2013; Wang and Toigo 2016). The discrepancy emerges based on the definition of the BTEC and the specific periods of the eddies analyzed. If BTEC is defined as the interaction between short-period ($1.5 < P < 8$ sol) eddies and the mean flow, plus the interaction between short-period eddies with other period eddies and curvature, the total BTEC is negative; short-period eddies lose energy barotropically. Individually, short-period eddies gain eddy kinetic energy from the mean flow (Battalio et al. 2018b,a) but lose eddy kinetic energy to other period eddies and curvature (Fig. 9). Separately, long-period eddies ($P > 8$ sol) gain energy from both the mean flow and short-period eddies (not shown). In combination, barotropic conversion is a source of energy for all eddies with a period of $P > 1.5$ (Tabataba-Vakili et al. 2015), but the short-period eddies gain energy from the mean flow only to lose a larger amount to other eddies.

Further work will analyze the energetics of Mars's transient waves by zonal wavenumber, applying the analysis of Battalio and Wang (2020) to a full energetics perspective to assess interannual variability. An open question is the precise nature of the solstitial pause, with regard to reductions in baroclinic activity being an intrinsic property of storm tracks. Cross-frequency eddy interactions remove short-period eddy energy; future research will investigate the energetics of long-period eddies ($8 < P < 30$) to better understand their growth and decay mechanisms and their relationship to both large dust events and the barotropically unstable, annular polar vortex. Quantification of the agreement between reanalysis datasets may provide the community an objective way to evaluate when the reanalyses are most likely to represent the true atmospheric state. Finally, a more comprehensive analysis of dust activity from the Mars Dust Activity Database (Battalio and Wang 2021) and their incipient transient waves may provide better diagnostic evidence of dust and wave evolution.

Acknowledgments. Comments by Juan M. Lora and three anonymous reviewers greatly improved the presentation and clarity of the paper. Conversations with Lenka Novak and Lina Boljka on Earth's storm tracks provided helpful insights into Mars's transient eddies.

Data availability statement. The Mars Analysis Correction Data Assimilation (v1.0) is available at https://doi.org/10.5285/78114093-E2BD-4601-8AE5-3551E62AEF2B. The Ensemble Mars Atmospheric Reanalysis System (v1.0) is available at https://doi.org/10.18113/D3W375. The Open access to Mars Assimilated Remote Soundings reanalysis (v1.0) is available at https://doi.org/10.21954/ou.rd.c.4278950. The Mars Dust Activity Database (v1.0) is available at https://doi.org/10.7910/DVN/F8R2JX.

REFERENCES

Banfield, D., B. Conrath, P. Gierasch, R. Wilson, and M. Smith, 2004: Traveling waves in the Martian atmosphere from MGS TES nadir data. *Icarus*, **170**, 365–403, https://doi.org/10.1016/j.icarus.2004.03.015.

Barnes, J. R., 1980: Time spectral analysis of midlatitude disturbances in the Martian atmosphere. *J. Atmos. Sci.*, **37**, 2002–2015, https://doi.org/10.1175/1520-0469(1980)037<2002:TSAOMD>2.0.CO;2.

——, 1981: Midlatitude disturbances in the Martian atmosphere: A second Mars year. *J. Atmos. Sci.*, **38**, 225–234, https://doi.org/10.1175/1520-0469(1981)038<0225:MDITMA>2.0.CO;2.

——, 1984: Linear baroclinic instability in the Martian atmosphere. *J. Atmos. Sci.*, **41**, 1536–1550, https://doi.org/10.1175/1520-0469(1984)041<1536:LBIITM>2.0.CO;2.

——, J. B. Pollack, R. M. Haberle, C. B. Leovy, R. W. Zurek, H. Lee, and J. Schaeffer, 1993: Mars atmospheric dynamics as simulated by the NASA Ames general circulation model 2. Transient baroclinic eddies. *J. Geophys. Res.*, **98**, 3125–3148, https://doi.org/10.1029/92JE02935.

——, R. M. Haberle, R. J. Wilson, S. R. Lewis, J. R. Murphy, and P. L. Read, 2017: The global circulation. *The Atmosphere and Climate of Mars*, R. M. Haberle et al., Eds., Cambridge University Press, 229–294, https://doi.org/10.1017/9781139060172.009.

Battalio, J. M., 2017: Wave energetics of the atmosphere of Mars. Ph.D. dissertation, Texas A&M University, 205 pp., https://hdl.handle.net/1969.1/161620.

——, and J. Dyer, 2017: The minimum length scale for evaluating QG omega using high-resolution model data. *Mon. Wea. Rev.*, **145**, 1659–1678, https://doi.org/10.1175/MWR-D-16-0241.1.

——, and H. Wang, 2019: The Aonia-Solis-Valles dust storm track in the Southern Hemisphere of Mars. *Icarus*, **321**, 367–378, https://doi.org/10.1016/j.icarus.2018.10.026.

——, and ——, 2020: Eddy evolution during large dust storms. *Icarus*, **338**, 113507, https://doi.org/10.1016/j.icarus.2019.113507.

——, and ——, 2021: The Mars Dust Activity Database (MDAD): A comprehensive statistical study of dust storm sequences. *Icarus*, **354**, 114059, https://doi.org/10.1016/j.icarus.2020.114059.

——, I. Szunyogh, and M. Lemmon, 2016: Energetics of the Martian atmosphere using the Mars Analysis Correction Data Assimilation (MACDA) dataset. *Icarus*, **276**, 1–20, https://doi.org/10.1016/j.icarus.2016.04.028.

——, ——, and ——, 2018a: Corrigendum to "Energetics of the Martian atmosphere using the Mars Analysis Correction Data Assimilation (MACDA) dataset." *Icarus*, **302**, 565–567, https://doi.org/10.1016/j.icarus.2017.10.001.

——, ——, and ——, 2018b: Wave energetics of the Southern Hemisphere of Mars. *Icarus*, **309**, 220–240, https://doi.org/10.1016/j.icarus.2018.03.015.

Cantor, B. A., 2007: MOC observations of the 2001 Mars planet-encircling dust storm. *Icarus*, **186**, 60–96, https://doi.org/10.1016/j.icarus.2006.08.019.

Chang, E. K. M., 1993: Downstream development of baroclinic waves as inferred from regression analysis. *J. Atmos. Sci.*, **50**, 2038–2053, https://doi.org/10.1175/1520-0469(1993)050<2038:DDOBWA>2.0.CO;2.

——, 2000: Wave packets and life cycles of troughs in the upper troposphere: Examples from the Southern Hemisphere summer season of 1984/85. *Mon. Wea. Rev.*, **128**, 25–50, https://doi.org/10.1175/1520-0493(2000)128<0025:WPALCO>2.0.CO;2.

——, S. Lee, and K. L. Swanson, 2002: Storm track dynamics. *J. Climate*, **15**, 2163–2183, https://doi.org/10.1175/1520-0442(2002)015<02163:STD>2.0.CO;2.

Collins, M., S. R. Lewis, and P. L. Read, 1996: Baroclinic wave transitions in the Martian atmosphere. *Icarus*, **120**, 344–357, https://doi.org/10.1006/icar.1996.0055.

Deng, Y., and T. Jiang, 2011: Intraseasonal modulation of the North Pacific storm track by tropical convection in boreal winter. *J. Climate*, **24**, 1122–1137, https://doi.org/10.1175/2010JCLI3676.1.

Diniz, F. L., and R. Todling, 2020: Assessing the impact of observations in a multi-year reanalysis. *Quart. J. Roy. Meteor. Soc.*, **146**, 724–747, https://doi.org/10.1002/qj.3705.

Egger, J., K. Weickmann, and K. P. Hoinka, 2007: Angular momentum in the global atmospheric circulation. *Rev. Geophys.*, **45**, RG4007, https://doi.org/10.1029/2006RG000213.

Forget, F., and Coauthors, 1999: Improved general circulation models of the Martian atmosphere from the surface to above 80 km. *J. Geophys. Res.*, **104**, 24 155–24 175, https://doi.org/10.1029/1999JE001025.

Greybush, S. J., R. J. Wilson, R. N. Hoffman, M. J. Hoffman, T. Miyoshi, K. Ide, T. McConnochie, and E. Kalnay, 2012: Ensemble Kalman filter data assimilation of thermal emission spectrometer temperature retrievals into a Mars GCM. *J. Geophys. Res.*, **117**, E11008, https://doi.org/10.1029/2012JE004097.

——, E. Kalnay, M. J. Hoffman, and R. J. Wilson, 2013: Identifying Martian atmospheric instabilities and their physical origins using bred vectors. *Quart. J. Roy. Meteor. Soc.*, **139**, 639–653, https://doi.org/10.1002/qj.1990.

——, H. E. Gillespie, and R. J. Wilson, 2019a: Transient eddies in the TES/MCS Ensemble Mars Atmosphere Reanalysis System (EMARS). *Icarus*, **317**, 158–181, https://doi.org/10.1016/j.icarus.2018.07.001.

——, and Coauthors, 2019b: The Ensemble Mars Atmosphere Reanalysis System (EMARS) version 1.0. *Geosci. Data J.*, **6**, 137–150, https://doi.org/10.1002/gdj3.77.

Hayashi, Y., and D. G. Golder, 1983: Transient planetary waves simulated GFDL spectral general circulation models. Part II: Effect of nonlinear energy transfer. *J. Atmos. Sci.*, **40**, 951–957, https://doi.org/10.1175/1520-0469(1983)040<0951:TPWSBG>2.0.CO;2.

Hinson, D. P., 2006: Radio occultation measurements of transient eddies in the Northern Hemisphere of Mars. *J. Geophys. Res.*, **111**, E05002, https://doi.org/10.1029/2005JE002612.

——, and H. Wang, 2010: Further observations of regional dust storms and baroclinic eddies in the Northern Hemisphere of Mars. *Icarus*, **206**, 290–305, https://doi.org/10.1016/j.icarus.2009.08.019.

——, and R. J. Wilson, 2021: Baroclinic waves in the Northern Hemisphere of Mars as observed by the MRO Mars Climate Sounder and the MGS Thermal Emission Spectrometer. *Icarus*, **357**, 114152, https://doi.org/10.1016/j.icarus.2020.114152.

——, H. Wang, and M. D. Smith, 2012: A multi-year survey of dynamics near the surface in the Northern Hemisphere of Mars: Short-period baroclinic waves and dust storms. *Icarus*, **219**, 307–320, https://doi.org/10.1016/j.icarus.2012.03.001.

Hollingsworth, J. L., and J. R. Barnes, 1996: Forced stationary planetary waves in Mars's winter atmosphere. *J. Atmos. Sci.*, **53**, 428–448, https://doi.org/10.1175/1520-0469(1996)053<0428:FSPWIM>2.0.CO;2.

——, and M. A. Kahre, 2010: Extratropical cyclones, frontal waves, and Mars dust: Modeling and considerations. *Geophys. Res. Lett.*, **37**, L22202, https://doi.org/10.1029/2010GL044262.

——, R. M. Haberle, J. R. Barnes, A. F. C. Bridger, J. B. Pollack, H. Lee, and J. Schaeffer, 1996: Orographic control of storm zones on Mars. *Nature*, **380**, 413–416, https://doi.org/10.1038/380413a0.

——, ——, and J. Schaeffer, 1997: Seasonal variations of storm zones on Mars. *Adv. Space Res.*, **19**, 1237–1240, https://doi.org/10.1016/S0273-1177(97)00275-5.

Holmes, J. A., S. R. Lewis, and M. R. Patel, 2020: OpenMARS: A global record of Martian weather from 1999 to 2015. *Planet. Space Sci.*, **188**, 104962, https://doi.org/10.1016/j.pss.2020.104962.

Jiang, T., Y. Deng, and W. Li, 2013: Local kinetic energy budget of high-frequency and intermediate-frequency eddies: Winter climatology and interannual variability. *Climate Dyn.*, **41**, 961–976, https://doi.org/10.1007/s00382-013-1684-1.

Kass, D. M., A. Kleinböhl, D. J. McCleese, J. T. Schofield, and M. D. Smith, 2016: Interannual similarity in the Martian atmosphere during the dust storm season. *Geophys. Res. Lett.*, **43**, 6111–6118, https://doi.org/10.1002/2016GL068978.

Kleinböhl, A., and Coauthors, 2009: Mars climate sounder limb profile retrieval of atmospheric temperature, pressure, and dust and water ice opacity. *J. Geophys. Res.*, **114**, E10006, https://doi.org/10.1029/2009JE003358.

Kuroda, T., A. S. Medvedev, P. Hartogh, and M. Takahashi, 2007: Seasonal changes of the baroclinic wave activity in the Northern Hemisphere of Mars simulated with a GCM. *Geophys. Res. Lett.*, **34**, L09203, https://doi.org/10.1029/2006GL028816.

Lee, C., M. I. Richardson, C. E. Newman, and A. Michael, 2018: The sensitivity of solsticial pauses to atmospheric ice and dust in the MarsWRF general circulation model. *Icarus*, **311**, 23–34, https://doi.org/10.1016/j.icarus.2018.03.019.

Lee, S., and I. M. Held, 1993: Baroclinic wave packets in models and observations. *J. Atmos. Sci.*, **50**, 1413–1428, https://doi.org/10.1175/1520-0469(1993)050<1413:BWPIMA>2.0.CO;2.

Lewis, S. R., P. L. Read, B. J. Conrath, J. C. Pearl, and M. D. Smith, 2007: Assimilation of thermal emission spectrometer atmospheric data during the Mars global surveyor aerobraking period. *Icarus*, **192**, 327–347, https://doi.org/10.1016/j.icarus.2007.08.009.

——, D. P. Mulholland, P. L. Read, L. Montabone, R. J. Wilson, and M. D. Smith, 2016: The solsticial pause on Mars: 1. A planetary wave reanalysis. *Icarus*, **264**, 456–464, https://doi.org/10.1016/j.icarus.2015.08.039.

McLay, J. G., and J. E. Martin, 2002: Surface cyclolysis in the North Pacific Ocean. Part III: Composite local energetics of tropospheric-deep cyclone decay associated with rapid surface cyclolysis. *Mon. Wea. Rev.*, **130**, 2507–2529, https://doi.org/10.1175/1520-0493(2002)130<2507:SCITNP>2.0.CO;2.

Montabone, L., and Coauthors, 2014: The Mars Analysis Correction Data Assimilation (MACDA) dataset V1.0. *Geosci. Data J.*, **1**, 129–139, https://doi.org/10.1002/gdj3.13.

——, and Coauthors, 2015: Eight-year climatology of dust optical depth on Mars. *Icarus*, **251**, 65–95, https://doi.org/10.1016/j.icarus.2014.12.034.

——, A. Spiga, D. M. Kass, A. Kleinböhl, F. Forget, and E. Millour, 2020: Martian year 34 column dust climatology from Mars Climate Sounder observations: Reconstructed maps and model simulations. *J. Geophys. Res. Planets*, **125**, e2019JE006111, https://doi.org/10.1029/2019JE006111.

Mooring, T. A., and R. J. Wilson, 2015: Transient eddies in the MACDA Mars reanalysis. *J. Geophys. Res. Planets*, **120**, 1671–1696, https://doi.org/10.1002/2015JE004824.

——, I. M. Held, and R. J. Wilson, 2019: Effects of the mean flow on Martian transient eddy activity: Studies with an idealized general circulation model. *J. Atmos. Sci.*, **76**, 2375–2397, https://doi.org/10.1175/JAS-D-18-0247.1.

Mulholland, D. P., S. R. Lewis, P. L. Read, J.-B. Madeleine, and F. Forget, 2016: The solsticial pause on Mars: 2 modelling and investigation of causes. *Icarus*, **264**, 465–477, https://doi.org/10.1016/j.icarus.2015.08.038.

Nakamura, H., 1992: Midwinter suppression of baroclinic wave activity in the Pacific. *J. Atmos. Sci.*, **49**, 1629–1642, https://doi.org/10.1175/1520-0469(1992)049<1629:MSOBWA>2.0.CO;2.

Novak, L., T. Schneider, and F. Ait-Chaalal, 2020: Midwinter suppression of storm tracks in an idealized zonally symmetric setting. *J. Atmos. Sci.*, **77**, 297–313, https://doi.org/10.1175/JAS-D-18-0353.1.

Oort, A. H., 1964: On estimates of the atmospheric energy cycle. *Mon. Wea. Rev.*, **92**, 483–493, https://doi.org/10.1175/1520-0493(1964)092<0483:OEOTAE>2.3.CO;2.

Orlanski, I., and J. Katzfey, 1991: The life cycle of a cyclone wave in the Southern Hemisphere. Part I: Eddy energy budget. *J. Atmos. Sci.*, **48**, 1972–1998, https://doi.org/10.1175/1520-0469(1991)048<1972:TLCOAC>2.0.CO;2.

——, and E. K. M. Chang, 1993: Ageostrophic geopotential fluxes in downstream and upstream development of baroclinic waves. *J. Atmos. Sci.*, **50**, 212–225, https://doi.org/10.1175/1520-0469(1993)050<0212:AGFIDA>2.0.CO;2.

Pankine, A. A., 2015: The nature of the systematic radiometric error in the MGS TES spectra. *Planet. Space Sci.*, **109–110**, 64–75, https://doi.org/10.1016/j.pss.2015.01.022.

——, 2016: Radiometric error and re-calibration of the MGS TES spectra. *Planet. Space Sci.*, **134**, 112–121, https://doi.org/10.1016/j.pss.2016.10.015.

Park, H. J., and K. Y. Kim, 2021: Influence of Northern Hemispheric winter warming on the Pacific storm track. *Climate Dyn.*, **56**, 1487–1506, https://doi.org/10.1007/s00382-020-05544-4.

Read, P. L., and S. R. Lewis, 2004: Transient weather systems. *The Martian Climate Revisited—Atmosphere and Environment of a Desert Planet*, Springer-Verlag, 137–178.

Rogberg, P., P. L. Read, S. R. Lewis, and L. Montabone, 2010: Assessing atmospheric predictability on Mars using numerical weather prediction and data assimilation. *Quart. J. Roy. Meteor. Soc.*, **136**, 1614–1635, https://doi.org/10.1002/qj.677.

Seviour, W. J. M., D. W. Waugh, and R. K. Scott, 2017: The stability of Mars's annular polar vortex. *J. Atmos. Sci.*, **74**, 1533–1547, https://doi.org/10.1175/JAS-D-16-0293.1.

Shirley, J. H., and Coauthors, 2015: Temperatures and aerosol opacities of the Mars atmosphere at aphelion: Validation and inter-comparison of limb sounding profiles from MRO/MCS and MGS/TES. *Icarus*, **251**, 26–49, https://doi.org/10.1016/j.icarus.2014.05.011.

Smith, M. D., 2004: Interannual variability in TES atmospheric observations of Mars during 1999–2003. *Icarus*, **167**, 148–165, https://doi.org/10.1016/j.icarus.2003.09.010.

——, 2009: THEMIS observations of Mars aerosol optical depth from 2002–2008. *Icarus*, **202**, 444–452, https://doi.org/10.1016/j.icarus.2009.03.027.

Szunyogh, I., 2014: Perturbation dynamics. *Applicable Atmospheric Dynamics*, World Scientific, 189–285, https://doi.org/10.1142/9789814335706_0002.

Tabataba-Vakili, F., P. L. Read, S. R. Lewis, L. Montabone, T. Ruan, Y. Wang, A. Valeanu, and R. M. B. Young, 2015: A Lorenz/Boer energy budget for the atmosphere of Mars from a "reanalysis" of spacecraft observations. *Geophys. Res. Lett.*, **42**, 8320–8327, https://doi.org/10.1002/2015GL065659.

Toigo, A. D., D. W. Waugh, and S. D. Guzewich, 2017: What causes Mars' annular polar vortices? *Geophys. Res. Lett.*, **44**, 71–78, https://doi.org/10.1002/2016GL071857.

Ulbrich, U., and P. Speth, 1991: The global energy cycle of stationary and transient atmospheric waves: Results from ECMWF analyses. *Meteor. Atmos. Phys.*, **45**, 125–138, https://doi.org/10.1007/BF01029650.

Wang, H., and M. I. Richardson, 2015: The origin, evolution, and trajectory of large dust storms on Mars during Mars years 24–30 (1999–2011). *Icarus*, **251**, 112–127, https://doi.org/10.1016/j.icarus.2013.10.033.

——, and A. D. Toigo, 2016: The variability, structure and energy conversion of the Northern Hemisphere traveling waves simulated in a Mars general circulation model. *Icarus*, **271**, 207–221, https://doi.org/10.1016/j.icarus.2016.02.005.

——, M. I. Richardson, R. J. Wilson, A. P. Ingersoll, A. D. Toigo, and R. W. Zurek, 2003: Cyclones, tides, and the origin of a cross-equatorial dust storm on Mars. *Geophys. Res. Lett.*, **30**, 1488, https://doi.org/10.1029/2002GL016828.

——, ——, A. D. Toigo, and C. E. Newman, 2013: Zonal wavenumber three traveling waves in the Northern Hemisphere of Mars simulated with a general circulation model. *Icarus*, **223**, 654–676, https://doi.org/10.1016/j.icarus.2013.01.004.

Waugh, D. W., A. D. Toigo, S. D. Guzewich, S. J. Greybush, R. J. Wilson, and L. Montabone, 2016: Martian polar vortices: Comparison of reanalyses. *J. Geophys. Res. Planets*, **121**, 1770–1785, https://doi.org/10.1002/2016JE005093.

Wilson, R. J., and K. Hamilton, 1996: Comprehensive model simulation of thermal tides in the Martian atmosphere. *J. Atmos. Sci.*, **53**, 1290–1326, https://doi.org/10.1175/1520-0469(1996)053<1290:CMSOTT>2.0.CO;2.

——, D. Banfield, B. J. Conrath, and M. D. Smith, 2002: Traveling waves in the Northern Hemisphere of Mars. *Geophys. Res. Lett.*, **29**, 1684, https://doi.org/10.1029/2002GL014866.

Xiao, J., K.-C. Chow, and K.-L. Chan, 2019: Dynamical processes of dust lifting in the northern mid-latitude region of Mars during the dust storm season. *Icarus*, **317**, 94–103, https://doi.org/10.1016/j.icarus.2018.07.020.